JM PAPERS

Shape dynamics and rheology of dilute suspensions of elastic and viscoelastic particles

Phani Kanth Sanagavarapu[1], Ganesh Subramanian[2] and Prabhu R. Nott[1],†

[1]Department of Chemical Engineering, Indian Institute of Science, Bangalore 560012, India

[2]Engineering Mechanics Unit, Jawaharlal Nehru Centre for Advanced Scientific Research, Bangalore 560064, India

This paper examines the shape dynamics of deformable elastic and viscoelastic particles in an ambient Newtonian fluid subjected to simple shear. The particles are allowed to undergo large deformation, with the elastic stress determined using the neo-Hookean constitutive relation. We first present a method to determine the shape dynamics of initially ellipsoidal particles that is an extension of the method of Roscoe (*J. Fluid Mech.*, vol. 28, issue 2, 1967, pp. 273–293), originally used to determine the shape at steady state of an initially spherical particle. We show that our method recovers earlier results for the in-plane trembling and tumbling dynamics of initially prolate spheroids in simple shear flow, obtained by a different approach. We then examine the in-plane dynamics of oblate spheroids and triaxial ellipsoids in simple shear flow, and show that they too, like prolate spheroids, exhibit time-periodic tumbling or trembling dynamics, depending on the initial aspect ratios of the particle and the elastic capillary number $G \equiv \mu\dot{\gamma}/\eta$, where μ is the viscosity of the fluid, η is the elastic shear modulus of the particle and $\dot{\gamma}$ is the shear rate. In addition, we find a novel state wherein the particle extends indefinitely in time and asymptotically aligns with the flow axis. We demarcate all the dynamical regimes in the parameter space comprising G and the initial particle aspect ratios. When the particles are viscoelastic, damped oscillatory dynamics is observed for initially spherical particles, and the tumbling–trembling boundary is altered for initially prolate spheroids so as to favour tumbling.

Key words: suspensions, rheology, capsule/cell dynamics

† Email address for correspondence: prnott@iisc.ac.in

1. Introduction

The rheology of a suspension of rigid particles in a Newtonian fluid has been well studied analytically (Einstein 1906; Batchelor & Green 1972; Brenner 1974; Dabade, Marath & Subramanian 2016), experimentally (Krieger 1972; de Kruif *et al.* 1985; Van der Werff & De Kruif 1989; Zarraga, Hill & Leighton 2000; Singh & Nott 2003; Snook *et al.* 2014) and computationally (Bossis & Brady 1984; Ladd 1994; Singh & Nott 2000; Gallier *et al.* 2014; Butler & Snook 2018). However, there are many examples of suspensions in nature and in industrial settings wherein the suspended particles are deformable, in the form of fluid droplets, vesicles, capsules or elastic particles; blood is an example of such a suspension, comprising cells of a range of deformability. In these cases, an imposed shear flow causes the particles to change shape, and determination of their evolving shapes is central to determining the rheology of the suspension. Even for suspensions that are dilute enough that interaction between particles may be ignored, the rheology is non-Newtonian due to the deformation of an isolated particle caused by the imposed flow. The shape dynamics of fluid droplets and its influence on the suspension rheology has been studied for several decades (Oldroyd 1953; Cox 1969; Stone 1994; Wetzel & Tucker 2001; Jackson & Tucker 2003; Minale 2010; Mwasame, Wagner & Beris 2017). In recent years, more attention has been devoted to the dynamics of vesicles and capsules (Kraus *et al.* 1996; Rioual, Biben & Misbah 2004; Kantsler & Steinberg 2006; Misbah 2006; Danker *et al.* 2007; Danker & Misbah 2007; Noguchi & Gompper 2007; Zhao & Shaqfeh 2011; Guedda, Benlahsen & Misbah 2014).

Most of the studies on deformable elastic and viscoelastic particles are restricted to the small deformation regime, wherein the constitutive relation for the elastic stress is effectively linear (Fröhlich & Sack 1946; Cerf 1952; Goddard & Miller 1967). The first systematic investigation of finite and large deformation of viscoelastic particles suspended in a Newtonian fluid was presented by Roscoe (1967), who used the neo-Hookean and Mooney–Rivlin constitutive models for the elastic stress. Roscoe's study was confined to the steady conformation (shape and orientation) of particles that are initially spherical (i.e. before shear is commenced). With the assumption that the particle undergoes homogeneous deformation in an ambient linear flow (where the undisturbed strain rate $\dot{\gamma}$ is a constant), Roscoe deduced that the particle traverses a sequence of ellipsoidal shapes with changing aspect ratios and orientation, as shown in figure 1, until a steady conformation is reached. At steady state, material points within the ellipsoidal particle execute a 'tank-treading' motion. Making use of Jeffery's result for the fluid velocity field around a rigid ellipsoid (Jeffery 1922) and imposing continuity of traction at the particle surface, the particle shape and its contribution to the suspension stress were determined in terms of the elastic capillary number $G \equiv \mu\dot{\gamma}/\eta$, where μ and η are the viscosity of the suspending fluid and the elastic shear modulus of the particle, respectively. The existence of the tank-treading steady state was numerically verified in two (circles; see Gao & Hu 2009) and three dimensions (spheres; see Gao, Hu & Castañeda 2011), thereby validating the assumption of homogeneous deformation by Roscoe (1967).

Gao *et al.* (2011) developed a semi-analytical method for determining the shape dynamics of elastic ellipsoids obeying the neo-Hookean constitutive relation, but restricted attention to initially spherical particles. The analysis was extended to prolate spheroids whose symmetry axis is in the plane of shear by Gao, Hu & Castaneda (2012). Using the stress polarization technique introduced by Eshelby (1957, 1959) for an elastic inclusion in an elastic matrix, the authors related the time derivative of the stress to the strain rate and vorticity fields inside the elastic particle through fourth-order shape tensors. The method yields a set of coupled nonlinear ordinary differential equations for the aspect
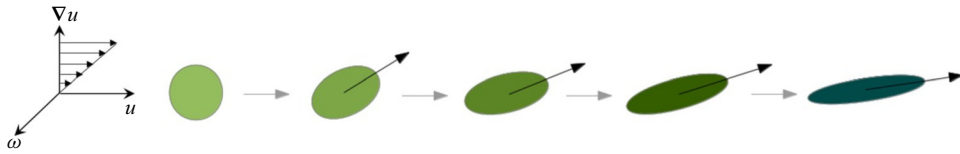
Figure 1. Soft elastic particle deforming through a series of ellipsoidal shapes due to applied shear. The intensity of colour indicates the magnitude of the stress along the major axis of the ellipsoid.

ratios, orientation and the (three) stress components, which was solved numerically to obtain the transient response. An important aspect of this study is that, in addition to the tumbling motion expected in the near-rigid (small G) limit, the authors showed the presence of a novel trembling motion that had earlier been observed in vesicles (Kantsler & Steinberg 2006; Misbah 2006; Zhao & Shaqfeh 2011) and further, determined the tumbling–trembling phase diagram in the G–ω_0 plane.

A key step in the method of Gao *et al.* (2011, 2012) is to obtain a relation between the time derivative of the stress and the strain rate by taking the upper convected time derivative of the neo-Hookean constitutive relation. However, for more general constitutive relations, such as Mooney–Rivlin, the time derivative of the stress cannot be related to the strain rate alone – the strain too will appear in the relation, thereby precluding the use of this method. It is therefore more appropriate to take the conventional approach in elasticity, where the stress is related to the strain or deformation. We show that the deformation at each instant of time can be obtained by recognizing that Roscoe's method (Roscoe 1967) for determining the stress in the fluid can be extended to dynamically evolving states; enforcing continuity of the traction at the particle surface gives relations for the strain rate and vorticity within the particle, which in turn are related to the time evolution of the shape and orientation. Importantly, this method provides physical insight into the nature of the shape dynamics. For instance, we see that the rate of change of orientation of the particle has two contributions, one due to vorticity-induced rotation and the other to stretching of the particle along a direction different from its principal axes. For simple shear flow, these two components are of opposite sign for a range of orientations, and their relative magnitudes decide whether a tumbling or trembling dynamics occurs; a steady state can be attained only when the two contributions are precisely balanced. Although we restrict our attention to the in-plane dynamics for the case of simple shear flow, wherein two principal axes of the spheroid are in the plane of shear, our approach is general enough that the dynamics resulting from arbitrary initial orientations can be obtained; the latter will be considered in a subsequent paper.

The following caveat must be made with regard to the solutions we obtain by assuming the particle to be ellipsoidal at all times (equivalently, assuming the stress and deformation in the particle to be always uniform). Eshelby (1957, 1959) showed that the ellipsoidal shape is the only solution for a linear elastic inclusion in a linear elastic medium; this was later extended to Newtonian drops in a Newtonian fluid by Wetzel & Tucker (2001). In both cases, the constitutive relations for the dispersed and continuous phases are linear. When the inclusion is a nonlinear elastic solid, it is not known *a priori* that the shape will be ellipsoidal. The only assertion we can make is that the assumption of ellipsoidal shape yields a solution – however, this need not be the only solution. Nevertheless, the numerical validation of Gao & Hu (2009); Gao *et al.* (2011) is an indication that the solutions are physically relevant ones.

The paper is organized as follows. In § 2, we present our method for determining the shape dynamics of an isolated ellipsoidal particle suspended in a Newtonian fluid whose

undisturbed flow is simple shear. The governing equations are then specialized for the in-plane dynamics of elastic and viscoelastic particles. In § 3, we solve the governing equations, where we first show that the results of Gao *et al.* (2012) for elastic spheres and prolate spheroids are recovered by our method (Appendix C). We then obtain the in-plane dynamics of elastic particles that are initially oblate spheroids or triaxial ellipsoids and construct the respective phase diagrams of dynamical states in the *G*–aspect ratio space. The effect of viscoelasticity on the shape dynamics is then discussed. We conclude in § 4 with a summary of our main findings, the inferences drawn from them, and the potential applications of our study.

2. Mathematical formulation

In this section, we derive the equations that govern the dynamics of the particle shape, orientation and stress. Our interest is in the dynamics of a dilute suspension of small particles of nominal size ℓ_p dispersed in viscous Newtonian liquids of density ρ and viscosity μ, with the suspension subjected to a uniform macroscopic strain rate. The bulk properties of such a suspension may be determined from the analysis of a single particle suspended in the fluid subjected to an undisturbed uniform strain rate of magnitude $\dot{\gamma}$. We further restrict attention to the flow regime where the Reynolds number $Re \equiv \rho\dot{\gamma}^2\ell_p^2/\mu$ is negligibly small. Therefore, we may ignore the effects of inertia and solve the quasistatic equations of motion in the fluid and the elastic particle.

Roscoe (1967) considered the steady shape and orientation of elastic and viscoelastic particles whose stress-free shape is a sphere. When the undisturbed strain rate in the fluid is spatially uniform, he hypothesized that the particle would approach the steady state by traversing a series of ellipsoidal shapes wherein the strain rate in the particle is uniform at every instant. At steady state, every material point must be in continuous motion along a closed elliptical path, i.e. the deformed particle executes a 'tank-treading' motion. We wish to determine the transient and unsteady dynamics of initially stress-free ellipsoidal particles, for which Roscoe's analysis is not directly applicable. However, an aspect of Roscoe's analysis, namely the determination of the fluid stress for a given shape and orientation of the ellipsoid, may be easily extended for dynamical states. We describe this aspect of Roscoe's analysis in § 2.1 and its extension to dynamical states in § 2.2. By enforcing continuity of traction on the particle surface, we relate the strain rate and vorticity in the particle to the stress at a given instant of time in § 2.2, and from them obtain relations for the shape dynamics in § 2.3. We then obtain the stress in the particle in terms of the incremental change in shape from the previous time instant in § 2.4, thereby closing the problem. The method described in this section for determining the shape dynamics is applicable for arbitrary linear velocity fields $\boldsymbol{u}^\infty$, but we consider only simple shear flow in this paper.

2.1. *Stress in the fluid*

Consider a neutrally buoyant deformable ellipsoidal particle suspended in an unbounded Newtonian fluid subjected to a uniform undisturbed velocity gradient $\boldsymbol{L}^\infty \equiv \nabla\boldsymbol{u}^\infty$. In the fixed laboratory Cartesian coordinate frame (figure 2), the only non-zero component of $\boldsymbol{L}^\infty$ for simple shear is $L_{12}^\infty = \dot{\gamma}$. We restrict attention to initial orientations where two principal axes of the ellipsoid are in the 1–2 plane; for spheroids one of them is the symmetry axis. From considerations of symmetry, these two principal axes will always remain in the 1–2 plane. However, our method is general and may also be used for the out-of-plane dynamics arising from the initial orientation not being in the 1–2 plane.
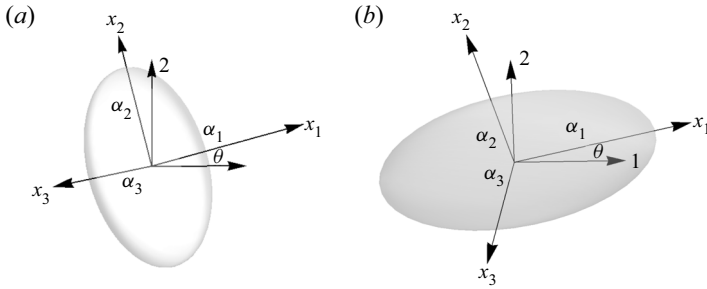
Figure 2. Schematic depicting the semi-axis lengths and orientations of the principal axes of a particle whose initial (stress free) shape is (*a*) an oblate spheroid and (*b*) prolate spheroid or triaxial ellipsoid. The axes labelled $(1, 2, x_3)$ are the coordinate axes in the fixed laboratory reference frame, and (x_1, x_2, x_3) are the principal axes of the particle. The aspect ratios of the particle are defined as $\omega_1 = \alpha_2/\alpha_1$, $\omega_2 = \alpha_3/\alpha_1$, where the α_i are the lengths of the principal semi-axes.

Hereafter, all the quantities of interest are quoted or reported in dimensionless form (unless specifically stated otherwise): the strain rate and vorticity are scaled by $\dot{\gamma}$, time by $\dot{\gamma}^{-1}$ and stress (in the fluid and particle) by $\mu\dot{\gamma}$. Let $\boldsymbol{D}^\infty$ and $\boldsymbol{W}^\infty$ denote the undisturbed strain rate and vorticity tensors, respectively. As argued by Roscoe (1967) (and validated numerically by Gao *et al.* 2011), the strain rate $\boldsymbol{D}$ and vorticity $\boldsymbol{W}$ in the particle vary in time but are spatially uniform. To determine the velocity and stress fields in the fluid, we follow Roscoe (1967) by subtracting $\boldsymbol{D}$ and $\boldsymbol{W}$, respectively, from the strain rate and vorticity at every point in the domain. As a result, the strain and vorticity fields now correspond to a rigid, non-rotating ellipsoid in a fluid of undisturbed strain rate $\boldsymbol{D}' \equiv \boldsymbol{D}^\infty - \boldsymbol{D}$ and vorticity $\boldsymbol{W}' \equiv \boldsymbol{W}^\infty - \boldsymbol{W}$. It follows from the linearity of Stokes equations that the velocity and stress fields in the fluid due to the deformable particle may be obtained by adding to the respective fields obtained for the above rigid particle problem, the contributions from the uniform strain rate and vorticity $\boldsymbol{D}$ and $\boldsymbol{W}$. As a result, the stress field in the fluid is

$$\boldsymbol{\sigma} = \boldsymbol{T}' + 2\boldsymbol{D}, \tag{2.1}$$

where $\boldsymbol{T}'$ is the stress field around a rigid, non-rotating ellipsoid in a fluid of undisturbed strain rate and vorticity $\boldsymbol{D}'$ and $\boldsymbol{W}'$, respectively. The expression for $\boldsymbol{T}'$ was given by Jeffery (1922), who studied the motion of rigid ellipsoidal particles in a Newtonian fluid subjected to homogeneous linear flow. Jeffery's expression was written compactly (with some errors in transcription corrected) by Roscoe (1967) as $\boldsymbol{T}' = -p'\boldsymbol{I} + \boldsymbol{A}'$, where p' is an arbitrary hydrostatic pressure and $\boldsymbol{A}'$ depends on the shape and orientation of the ellipsoid and linearly on $\boldsymbol{D}'$. Note that $\boldsymbol{A}'$ is not necessarily traceless. The arguments leading to (2.1) ensure continuity of velocity on the particle surface.

It is convenient to use a coordinate frame that is instantaneously aligned with the principal axes of the ellipsoid (see figure 2), in which the equation of the surface is

$$\frac{x_1^2}{\alpha_1^2} + \frac{x_2^2}{\alpha_2^2} + \frac{x_3^2}{\alpha_3^2} = 1, \tag{2.2}$$

where α_i are the lengths of the three principal semi-axes. The axis labels are chosen based on the initial shape: for oblate spheroids, the x_1 axis is the in-plane principal axis of smaller length. For prolate spheroids and triaxial ellipsoids, the x_1 axis is the in-plane principal axis of larger length. Thus, the x_1 axis for spheroids in the stress-free state coincides with the symmetry axis. The aspect ratios are defined as $\omega_1 = \alpha_2/\alpha_1$ and $\omega_2 = \alpha_3/\alpha_1$.

In the particle coordinate frame, the undisturbed strain rate and vorticity may be expressed in terms of the Euler angles measuring the orientation of the principal axes relative to the axes of the fixed laboratory frame. For the in-plane dynamics in simple shear, only the Euler angle in the plane of shear varies with time (the other two being zero) and the undisturbed strain rate and vorticity are

$$\boldsymbol{D}^{\infty} = \begin{bmatrix} \frac{1}{2}\sin 2\theta & \frac{1}{2}\cos 2\theta & 0 \\ \frac{1}{2}\cos 2\theta & \frac{-1}{2}\sin 2\theta & 0 \\ 0 & 0 & 0 \end{bmatrix}, \quad \boldsymbol{W}^{\infty} = \begin{bmatrix} 0 & \frac{1}{2} & 0 \\ \frac{-1}{2} & 0 & 0 \\ 0 & 0 & 0 \end{bmatrix}, \qquad (2.3a,b)$$

where θ is the angle subtended by the x_1 axis with the flow direction in the anti-clockwise direction (figure 2).

2.2. *Strain rate and vorticity in the particle*

To proceed further, we enforce continuity of traction at the particle surface

$$\boldsymbol{\sigma}^p \cdot \boldsymbol{n} = \boldsymbol{\sigma} \cdot \boldsymbol{n}, \qquad (2.4)$$

where $\boldsymbol{\sigma}^p$ is the (spatially uniform) stress in the particle and $\boldsymbol{n}$ is a unit vector normal to the surface. As $\boldsymbol{\sigma}^p$ is uniform, it suffices to enforce continuity of traction at the intersection of the ellipsoidal surface with each principal axis. From (2.1) and (2.4), continuity of the normal component of the traction $\boldsymbol{n} \cdot \boldsymbol{\sigma} \cdot \boldsymbol{n}$ at the intersection with the i axis gives

$$\sigma_{ii}^p = -p' + \hat{A}'_{ii} + 2D_{ii}, \qquad (2.5)$$

where $\hat{A}'_{ij}$ is the value of A'_{ij} at $x_i = \alpha_i$, $x_k = 0$ ($k \neq i$). The pressures p' in the fluid and p in the particle (see (2.18)) may be eliminated by taking differences between the normal traction at the intersections of the principal axes with the surface of the ellipsoid,

$$\sigma_{11}^p - \sigma_{22}^p = (\hat{A}'_{11} - \hat{A}'_{22}) + 2(D_{11} - D_{22}), \qquad (2.6a)$$

$$\sigma_{11}^p + \sigma_{22}^p - 2\sigma_{33}^p = (\hat{A}'_{11} + \hat{A}'_{22} - 2\hat{A}'_{33}) + 6(D_{11} + D_{22}). \qquad (2.6b)$$

The expression for $\hat{A}'_{11}$ is (Roscoe 1967)

$$\hat{A}'_{11} = \frac{4}{3} \frac{2g''_1(D'_{11} - D_{11}) - g''_2(D'_{22} - D_{22}) - g''_3(D'_{33} - D_{33})}{g''_1 g''_2 + g''_2 g''_3 + g''_3 g''_1}. \qquad (2.7)$$

The expressions for $\hat{A}'_{22}$ and $\hat{A}'_{33}$ are obtained by cyclic permutation of indices in (2.7). Here, g''_i are functions of the semi-axis lengths α_i defined by Roscoe (1967); they are reproduced in Appendix A for the convenience of the reader. For the state of steady orientation and shape, the terms D_{ii} in (2.5)–(2.7) should be set to zero (see (2.16)); this was the state considered by Roscoe. As we wish to determine the transient and unsteady dynamics, we must retain these terms.

Substituting the expressions for $\hat{A}'_{ii}$ in (2.6) and rearranging the terms, we get

$$\sigma^p_{11} - \sigma^p_{22} = 5((I_{12} + J_{12})\left(D^\infty_{11} - D_{11}\right)$$
$$+ (I_{12} - J_{12})\left(D^\infty_{22} - D_{22}\right)) + 2\left(D_{11} - D_{22}\right), \qquad (2.8a)$$

$$\sigma^p_{11} + \sigma^p_{22} - 2\sigma^p_{33} = 5((I_{12} + J_{12})\left(D^\infty_{11} - D_{11}\right) + (I_{12} - J_{12})\left(D^\infty_{22} - D_{22}\right)$$
$$+ 2\left(I_{23} - J_{23}\right)\left(\left(D^\infty_{11} - D_{11}\right) + \left(D^\infty_{22} - D_{22}\right)\right))$$
$$+ 6\left(D_{11} - D_{22}\right), \qquad (2.8b)$$

where,

$$I_{12} = \frac{2}{5}\frac{g''_1 + g''_2}{g}, \quad J_{12} = \frac{2}{5}\frac{g''_1 - g''_2}{g}, \qquad (2.9a)$$

$$I_{23} = \frac{2}{5}\frac{g''_2 + g''_3}{g}, \quad J_{23} = \frac{2}{5}\frac{g''_2 - g''_3}{g}, \qquad (2.9b)$$

and $g = g''_2 g''_3 + g''_3 g''_1 + g''_1 g''_2$. Explicit expressions for D_{11} and D_{22} are obtained by solving (2.8a,b) and are provided in Appendix B.

Continuity of the tangential component of the traction $t \cdot \boldsymbol{\sigma} \cdot n$, where t is a unit tangent on the 1-axis, gives

$$\sigma^p_{12} = \hat{A}'_{12} + 2D_{12}, \qquad (2.10)$$

where

$$\hat{A}'_{12} = \frac{8[g_1(D^\infty_{12} - D_{12}) + \alpha^2_2 g'_3(W^\infty_{12} - W_{12})]}{2g'_3(\alpha^2_1 g_1 + \alpha^2_2 g_2)}. \qquad (2.11)$$

The factors g_i and g'_i are functions of the semi-axis lengths α_i (Roscoe 1967) and are defined in Appendix A. Similarly, $\hat{A}'_{21}$ can be obtained by interchanging the indices 1 and 2 in (2.11). Symmetry of $\boldsymbol{\sigma}^p$ requires that $\hat{A}'_{12} = \hat{A}'_{21}$, which yields the relation

$$(g_1 - g_2)(D^\infty_{12} - D_{12}) = -(\alpha^2_1 + \alpha^2_2)g'_3(W^\infty_{12} - W_{12}). \qquad (2.12)$$

Noting that $g_1 - g_2 = (\alpha^2_1 - \alpha^2_2)g'_3$, (2.12) results in the following relation between the strain rate and the vorticity fields inside the particle:

$$(W^\infty_{12} - W_{12}) = \frac{(\alpha^2_1 - \alpha^2_2)}{(\alpha^2_1 + \alpha^2_2)}(D^\infty_{12} - D_{12}). \qquad (2.13)$$

Substituting (2.13) into the expression for $\hat{A}'_{12}$ and subsequently into (2.10) yields the expression for the shear stress in the 1–2 plane

$$\sigma^p_{12} = \frac{8\left[g_1 + \alpha^2_2 g'_3\left(\dfrac{\alpha^2_1 - \alpha^2_2}{\alpha^2_1 + \alpha^2_2}\right)\right](D^\infty_{12} - D_{12})}{2g'_3(\alpha^2_1 g_1 + \alpha^2_2 g_2)} + 2D_{12}. \qquad (2.14)$$

Expressions for σ^p_{23} and σ^p_{13} (needed only for the off-plane dynamics) may be obtained by cyclic permutation of indices in (2.14). Equations (2.13) and (2.14) provide the required relations for D_{12} and W_{12}; the expressions are lengthy and given in Appendix B.

Thus, with knowledge of the particle stress $\boldsymbol{\sigma}^p$, we can determine $\boldsymbol{D}$ and $\boldsymbol{W}$ in the particle. The determination of $\boldsymbol{\sigma}^p$ from the instantaneous orientation and shape of the particle, starting from the stress-free configuration at $t = 0$, is discussed in § 2.4.

2.3. *Evolution of particle shape and orientation*

The evolution of the shape and orientation can be obtained in terms of the strain rate and vorticity in the particle using the formulation of Wetzel & Tucker (2001). In the coordinate system instantaneously aligned with the particle principal axes at time t (but not co-rotating with it), the surface of the ellipsoid satisfies the equation $\boldsymbol{S} : \boldsymbol{xx} = 1$, where $\boldsymbol{S}$ is the diagonal shape tensor with components $S_{ii} = 1/\alpha_i^2$. Applying the material derivative to this equation and using the definition of the instantaneous velocity field inside the particle, $\boldsymbol{v} = \boldsymbol{L} \cdot \boldsymbol{x}$, where $\boldsymbol{L}$ is the uniform velocity gradient in the particle, the following relation can be obtained:

$$\frac{\mathrm{d}\boldsymbol{S}}{\mathrm{d}t} + \boldsymbol{L}^{\mathrm{T}} \cdot \boldsymbol{S} + \boldsymbol{S} \cdot \boldsymbol{L} = 0. \tag{2.15}$$

Note that $\mathrm{d}\boldsymbol{S}/\mathrm{d}t$ is not diagonal, as a result of particle rotation; it is obtained by replacing $\boldsymbol{S}$ by $\boldsymbol{S}' = \boldsymbol{R}(\theta) \cdot \boldsymbol{S} \cdot \boldsymbol{R}^{\mathrm{T}}(\theta)$, where $\boldsymbol{R}(\theta)$ is the rotation tensor corresponding to a rotation by angle θ in the 1–2 plane, taking the time derivative of $\boldsymbol{S}'$, and then setting θ to zero. Equation (2.15) is the only aspect of the analysis of Wetzel & Tucker (2001) that we use. In particular, we eschew using their method of writing the deformation rate and vorticity in the particle in terms of fourth rank 'concentration tensors', and use instead the more direct method described in § 2.2.

Substituting $\boldsymbol{L} = \boldsymbol{D} + \boldsymbol{W}$, the diagonal components of (2.15) give relations for the time evolution of the semi-axis lengths,

$$\frac{1}{\alpha_i} \frac{\mathrm{d}\alpha_i}{\mathrm{d}t} = D_{ii}, \tag{2.16}$$

and the off-diagonal 1–2 component yields the evolution equation for the orientation

$$\frac{\mathrm{d}\theta}{\mathrm{d}t} = \frac{\alpha_1^2 + \alpha_2^2}{\alpha_1^2 - \alpha_2^2} D_{12} - W_{12}. \tag{2.17}$$

At steady state, (2.17) yields the linear relation between D_{12} and W_{12} obtained by Roscoe (1967).

2.4. *Stress in the particle*

We model the particle as an incompressible neo-Hookean solid, satisfying the constitutive relation

$$\boldsymbol{\sigma}^p = -p\boldsymbol{I} + \boldsymbol{\tau} = -p\boldsymbol{I} + \eta\,(\boldsymbol{B} - \boldsymbol{I}), \tag{2.18}$$

where p is the pressure in the solid that varies so as to enforce incompressibility, $\boldsymbol{B}$ is the configuration dependent finger tensor (or the left Cauchy–Green deformation tensor) and η is the elastic modulus. The finger tensor is defined as $\boldsymbol{B} = \boldsymbol{F} \cdot \boldsymbol{F}^{\mathrm{T}}$, where $\boldsymbol{F} = \partial\boldsymbol{x}/\partial\boldsymbol{X}$ is the deformation gradient tensor relating the configuration at time t to the stress-free initial configuration. Note that (2.18) gives the stress in dimensional form; when scaled by $\mu\dot{\gamma}$ (see § 2.1), the dimensionless extra stress is $\boldsymbol{\tau} = (1/G)(\boldsymbol{B} - \boldsymbol{I})$, where $G \equiv \mu\dot{\gamma}/\eta$ is the elastic capillary number. Determination of the stress requires $\boldsymbol{F}$, which we determine below from the deformation history of the particle.

2.4.1. *Particle deformation in a small time interval δt*

Consider a time t_i at which the shape (α_1, α_2, α_3) and orientation (θ) of the particle are known (figure 3a). We determine the deformation in the time interval δt that is small
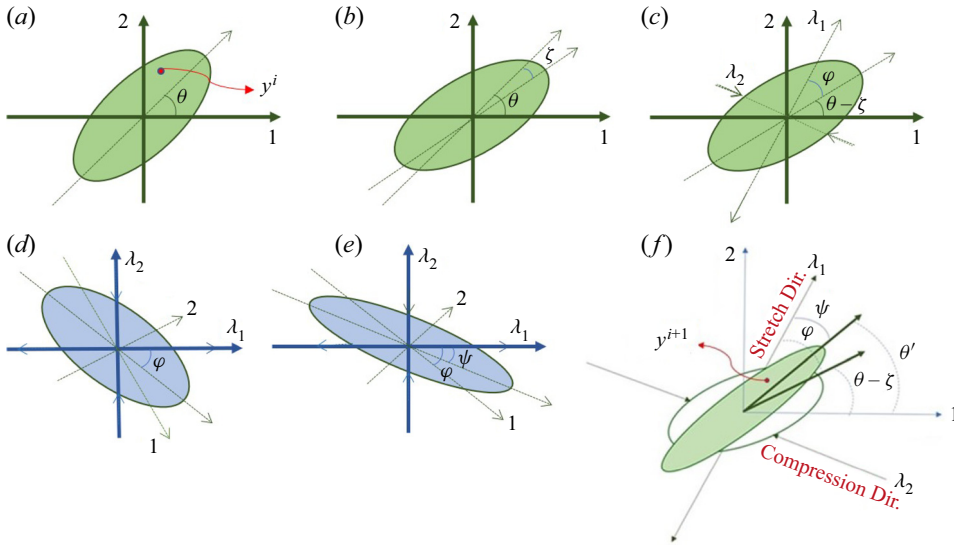
Figure 3. Sequence of steps involved in mapping a material point from time t_i to t_{i+1}. All angles are positive in the anti-clockwise direction. (*a*) Particle at initial orientation θ. (*b*) In-plane rotation of the particle due to the (uniform) vorticity field in the particle by an angle $-\zeta$. After rotation, the extensional stretch axis (λ_1 axis) subtends an angle φ with the x_1 axis of the particle. (*c*) Stretching of the particle due to the (uniform) strain rate at an angle φ from its principal axes. After stretching, the extensional stretch axis subtends an angle ψ with the x_1 axis. (*d,e*) Virtual transformations to effect stretching: in (*d*) the particle is rotated by $-(\theta - \zeta + \varphi)$ so that the stretch axes are aligned with the laboratory axes; in (*e*) the particle undergoes stretches of $\lambda_1, \lambda_2, \lambda_3$ along the laboratory axes. After stretching, it is rotated by $(\theta - \zeta + \varphi)$. (*f*) The conformation of the particle at t_{i+1}, after rotation and stretching.

enough that the stress in the particle can be assumed to remain constant. The particle undergoes an in-plane rotation through an angle $-\zeta$ due to vorticity (see figure 3*b*). It also undergoes deformation by in-plane stretches λ_1 and λ_2 ($\lambda_1 > \lambda_2$) (ratios of deformed lengths to original lengths of a differential material element) oriented at angles φ and $\varphi + \pi/2$, respectively, to the x_1 axis of the particle (see figure 3*c*); incompressibility requires the particle to be stretched by $\lambda_3 = 1/(\lambda_1\lambda_2)$ in the 3-direction. Due to the misalignment between the directions of stretch and the particle axes, the orientation further changes such that the extensional stretch axis (λ_1 axis) subtends an angle ψ with the x_1 axis (figure 3*f*). All angles are defined as positive in the anti-clockwise direction. Note that the angles of rotation ζ and $\psi - \varphi$, and the deviations of the stretches from unity $\lambda_1 - 1$ and $\lambda_2 - 1$ are all proportional to δt. As a result of the changes in orientation due to vorticity and stretch, the orientation θ' at $t_{i+1} = t_i + \delta t$ is

$$\theta' = \theta - \zeta + \varphi - \psi. \tag{2.19}$$

Following the rotation and stretch, the mapping between positions of a material point, expressed in the laboratory reference frame, at times t_i and t_{i+1} is

$$\boldsymbol{y}^{i+1} = \boldsymbol{R}(\theta - \zeta + \varphi) \cdot \boldsymbol{T} \cdot \boldsymbol{R}(-\theta + \zeta - \varphi) \cdot \boldsymbol{R}(-\zeta) \cdot \boldsymbol{y}^i, \tag{2.20}$$

where $\boldsymbol{T}$ is the diagonal stretch tensor with components $T_{ii} = \lambda_i$ and $\boldsymbol{R}$ is the rotation tensor defined in §2.3. The combination $\boldsymbol{R}(\theta - \zeta + \varphi) \cdot \boldsymbol{T} \cdot \boldsymbol{R}(-\theta + \zeta - \varphi)$ serves to transform the diagonal stretch tensor to the laboratory reference frame by accounting for the angle $\theta - \zeta + \varphi$ between the λ_1 axis of stretch and the flow direction (see figure 3*c*).

Equation (2.20) may be written as

$$y^{i+1} = F^i \cdot y^i, \tag{2.21}$$

where F^i is the deformation gradient tensor in the laboratory reference frame whose components have the values

$$
\left.
\begin{aligned}
F^i_{11} &= \tfrac{1}{2}\{(\lambda_1 + \lambda_2)\cos\zeta + (\lambda_1 - \lambda_2)\cos(2\theta + 2\varphi - \zeta)\}, \\
F^i_{12} &= \tfrac{1}{2}\{(\lambda_1 + \lambda_2)\sin\zeta + (\lambda_1 - \lambda_2)\sin(2\theta + 2\varphi - \zeta)\}, \\
F^i_{21} &= \tfrac{1}{2}\{-(\lambda_1 + \lambda_2)\sin\zeta + (\lambda_1 - \lambda_2)\sin(2\theta + 2\varphi - \zeta)\}, \\
F^i_{22} &= \tfrac{1}{2}\{(\lambda_1 + \lambda_2)\cos\zeta - (\lambda_1 - \lambda_2)\cos(2\theta + 2\varphi - \zeta)\} \\
F^i_{13} &= F^i_{23} = F^i_{31} = F^i_{32} = 0; \quad F^i_{33} = \lambda_3.
\end{aligned}
\right\} \tag{2.22}
$$

2.4.2. *Relating the shape and orientation to the strain rate and vorticity*

To evaluate F^i, we need the values of $\lambda_1, \lambda_2, \zeta, \varphi$ and ψ. From (2.17) and (2.19), the change in orientation due to vorticity and stretching, respectively, are given by

$$\zeta = W_{12}\,\delta t, \tag{2.23a}$$

$$\varphi - \psi = \left(\frac{\alpha_1^2 + \alpha_2^2}{\alpha_1^2 - \alpha_2^2}\right) D_{12}\,\delta t, \tag{2.23b}$$

with errors of $O(\delta t^2)$. An additional equation comes from the condition that there is no shear along the principal stretch directions. It then follows from Mohr's circle for the strain rate that

$$\varphi = \frac{1}{2}\tan^{-1}\frac{2D_{12}}{D_{11} - D_{22}}. \tag{2.24}$$

The relations (2.16) and (2.23) over the time step δt along with (2.24) give us updated lengths α_i of the semi-axes and the orientation θ', and the angles ζ, φ and ψ.

It now remains to calculate the stretches λ_1 and λ_2 to obtain the deformation gradient tensor. For this, we consider the shape of the particle after it is stretched by the principal stretch tensor T. Consider the particle in figure 3(d), where it has been rotated so that the principal stretch axes align with the laboratory axes. The equation of the in-plane cross-section of the particle in laboratory coordinates before stretching is that of an ellipse at an angle $-\varphi$ to the 1-axis. Stretching transforms each point (y_1, y_2, y_3) in the ellipsoid to $(\lambda_1 y_1, \lambda_2 y_2, \lambda_3 y_3)$, whence the equation of the cross-section after stretching is

$$
y_1^2\left(\frac{\cos^2\varphi}{\lambda_1^2\alpha_1^2} + \frac{\sin^2\varphi}{\lambda_1^2\alpha_2^2}\right) + y_2^2\left(\frac{\sin^2\varphi}{\lambda_2^2\alpha_1^2} + \frac{\cos^2\varphi}{\lambda_2^2\alpha_2^2}\right) - \frac{2y_1 y_2}{\lambda_1\lambda_2}\left(\frac{1}{\alpha_1^2} - \frac{1}{\alpha_2^2}\right)\sin\varphi\cos\varphi = 1.
\tag{2.25}
$$

The principal axis of the particle is now at an angle $-\psi$ to the 1-axis (figure 3e), and its semi-axis lengths have changed to $(\alpha_1', \alpha_2', \alpha_3')$, which are obtained by integrating (2.16)

949 A22-10

over the time interval δt. The equation of the cross-section can therefore be equivalently be written as

$$y_1^2 \left(\frac{\cos^2 \psi}{\alpha_1'^2} + \frac{\sin^2 \psi}{\alpha_2'^2} \right) + y_2^2 \left(\frac{\sin^2 \psi}{\alpha_1'^2} + \frac{\cos^2 \psi}{\alpha_2'^2} \right) - 2y_1 y_2 \left(\frac{1}{\alpha_1'^2} - \frac{1}{\alpha_2'^2} \right) \sin \psi \cos \psi = 1.$$

(2.26)

Comparing the coefficients of y_1^2 and y_2^2 in (2.25) and (2.26), we get the required expressions for λ_1 and λ_2

$$\lambda_1 = \left(\frac{\dfrac{\cos^2 \varphi}{\alpha_1^2} + \dfrac{\sin^2 \varphi}{\alpha_2^2}}{\dfrac{\cos^2 \psi}{\alpha_1'^2} + \dfrac{\sin^2 \psi}{\alpha_2'^2}} \right)^{1/2} , \quad \lambda_2 = \left(\frac{\dfrac{\sin^2 \varphi}{\alpha_1^2} + \dfrac{\cos^2 \varphi}{\alpha_2^2}}{\dfrac{\sin^2 \psi}{\alpha_1'^2} + \dfrac{\cos^2 \psi}{\alpha_2'^2}} \right)^{1/2} .$$

(2.27)

2.4.3. *Particle stress in terms of the kinematic variables*

The deformation gradient tensor F^i in (2.22) relates positions of material points in the laboratory coordinate system between times t_{i+1} and t_i. However, the constitutive relation for the elastic stress requires the deformation gradient F that relates the configuration at time t_{i+1} to the stress-free configuration at $t_0 = 0$. This is simply the time-ordered contraction of F^i at all intermediate states

$$F = F^i \cdot F^{i-1} \ldots \cdot F^1 \cdot F^0.$$

(2.28)

The finger tensor in the fixed laboratory coordinate frame then is $\boldsymbol{B}_{lab} = \boldsymbol{F} \cdot \boldsymbol{F}^{\mathrm{T}}$. As we require the particle stress in the coordinate system aligned with its principal axes (which subtend an angle of θ' with fixed laboratory coordinates),

$$\boldsymbol{B} = \boldsymbol{R}(-\theta') \cdot \boldsymbol{B}_{lab} \cdot \boldsymbol{R}(\theta')$$

(2.29)

is the appropriate finger tensor to determine the stress in (2.18).

2.5. *Extension to viscoelastic particles*

For a viscoelastic solid, the total stress is the sum of elastic and viscous contributions, $\boldsymbol{\sigma}^p = \boldsymbol{\sigma}^e + \boldsymbol{\sigma}^v$. Determination of the elastic stress $\boldsymbol{\sigma}^e$ has already been outlined in § 2.4; the viscous contribution is $\boldsymbol{\sigma}^v = 2\kappa \boldsymbol{D}$, where κ is the viscosity ratio of the particle to the fluid. Balancing the normal and tangential components of the traction at the surface of the particle, and following the same procedure as in § 2.2 to eliminate the pressure, we get the

following equations that extend (2.8) and (2.14) for a viscoelastic particle:

$$\sigma_{11}^p - \sigma_{22}^p = (\sigma_{11}^e - \sigma_{22}^e) + 2\kappa (D_{11} - D_{22})$$
$$= 5 \left((I_{12} + J_{12}) \left(D_{11}^\infty - D_{11} \right) + (I_{12} - J_{12}) \left(D_{22}^\infty - D_{22} \right) \right)$$
$$+ 2 (D_{11} - D_{22}), \tag{2.30a}$$

$$\sigma_{11}^p + \sigma_{22}^p - 2\sigma_{33}^p = (\sigma_{11}^e + \sigma_{22}^e - 2\sigma_{33}^e) + 6\kappa (D_{11} - D_{22})$$
$$= 5((I_{12} + J_{12}) \left(D_{11}^\infty - D_{11} \right) + (I_{12} - J_{12}) \left(D_{22}^\infty - D_{22} \right)$$
$$+ 2 (I_{23} - J_{23}) \left(\left(D_{11}^\infty - D_{11} \right) + \left(D_{22}^\infty - D_{22} \right) \right))$$
$$+ 6 (D_{11} - D_{22}), \tag{2.30b}$$

$$\sigma_{12}^p = \sigma_{12}^e + 2\kappa D_{12}$$
$$= \frac{8 \left[g_1 + \alpha_2^2 g_3' \left(\dfrac{\alpha_1^2 - \alpha_2^2}{\alpha_1^2 + \alpha_2^2} \right) \right] (D_{12}^\infty - D_{12})}{2 \, g_3'(\alpha_1^2 g_1 + \alpha_2^2 g_2)} + 2D_{12}. \tag{2.30c}$$

Again, cyclic permutation of indices in σ_{12}^p provides the expressions for σ_{23}^p and σ_{13}^p. The components of the strain rate and vorticity fields in the viscoelastic particle can be obtained by solving (2.30) and are given in § B.2 of Appendix B.

2.6. *Calculation of rheological properties*

The bulk stress in the suspension is $\langle \boldsymbol{\sigma} \rangle = \phi \langle \boldsymbol{\sigma} \rangle^p + (1 - \phi)\langle \boldsymbol{\sigma} \rangle^f$, where ϕ is the particle volume fraction and the angle brackets represent volume averages. Similarly, the bulk strain rate of the suspension can be expressed in terms of the respective averages in the two phases, $\langle \boldsymbol{D} \rangle = \phi \langle \boldsymbol{D} \rangle^p + (1 - \phi)\langle \boldsymbol{D} \rangle^f$. Therefore, the suspension stress is

$$\langle \sigma \rangle = -\langle p \rangle \boldsymbol{I} + 2\langle \boldsymbol{D} \rangle + \phi (\langle \boldsymbol{\tau} \rangle^p - 2\langle \boldsymbol{D} \rangle^p). \tag{2.31}$$

Note that the bulk strain rate and vorticity are identical to the externally imposed flow quantities, i.e. $\langle \boldsymbol{D} \rangle = \boldsymbol{D}^\infty$ and $\langle \boldsymbol{W} \rangle = \boldsymbol{W}^\infty$.

We consider the suspension to be composed of ellipsoids of identical size but different orientations in the initial (stress-free) state. As the suspension is dilute enough that particles do not interact, the undisturbed flow experienced by each particle is the imposed linear flow, for which the strain rate and stress within each particle at each instant of time are uniform. As a result, $\langle \boldsymbol{\tau}^p \rangle$ and $\langle \boldsymbol{D}^p \rangle$ represent averages over the orientation of a single particle. We find that the long-time orientation dynamics for initial ellipsoidal particles is identical, to within a phase lag, regardless of the initial orientation; the phase lag is a residual signature of the short transient associated with the stress-free initial orientation. Therefore, the long-time average for ellipsoids over all initial orientations is identical to the average over a time period of tumbling or trembling; for initially spherical particles it is trivially the steady state.

The rheological properties of interest then are the intrinsic shear viscosity

$$[\mu]_s = \frac{\dfrac{\langle \sigma \rangle_{12}}{2D_{12}^\infty} - 1}{\phi} = \langle \tau \rangle_{12}^p - 2\langle D \rangle_{12}^p, \tag{2.32}$$
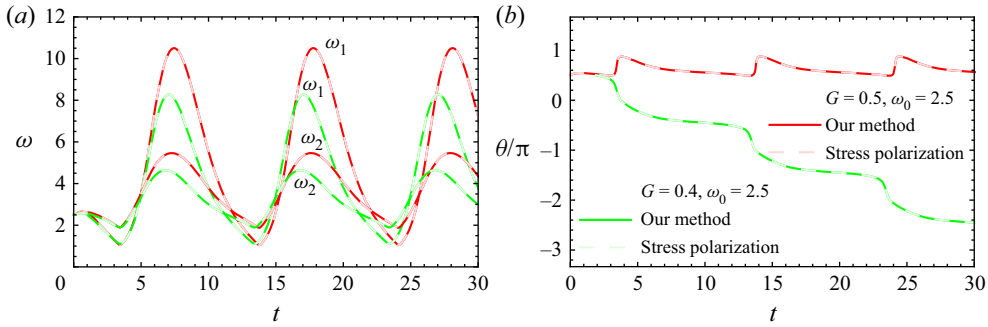
Figure 4. Dynamics of an initially oblate spheroid exhibiting trembling and tumbling dynamics at $\omega_0 = 2.5$. (*a*) In-plane and out-of-plane aspect ratios. (*b*) Orientation of the x_1 axis. The stress polarization results were obtained using the method of Gao *et al.* (2011).

and the intrinsic normal stress differences in simple shear flow

$$N_1 = \frac{\langle \sigma \rangle_{11} - \langle \sigma \rangle_{22}}{\phi} = (\langle \tau \rangle_{11}^p - \langle \tau \rangle_{22}^p) - 2(\langle D \rangle_{11}^p - \langle D \rangle_{22}^p), \tag{2.33a}$$

$$N_2 = \frac{\langle \sigma \rangle_{22} - \langle \sigma \rangle_{33}}{\phi} = (\langle \tau \rangle_{22}^p - \langle \tau \rangle_{33}^p) - 2(\langle D \rangle_{22}^p - \langle D \rangle_{33}^p). \tag{2.33b}$$

3. Results and discussion

3.1. *Dynamics of an elastic particle in simple shear flow*

We study the shape dynamics of neutrally buoyant elastic particles whose initial (stress-free) shape is a sphere, a spheroid and, more generally, a triaxial ellipsoid, suspended in an unbounded Newtonian fluid subjected to simple shear. As mentioned in § 1, the shape dynamics of an initial sphere and prolate spheroid were reported earlier by Gao *et al.* (2011, 2012). We validate our solution method by a comparison with their results; the comparison is provided in Appendix C, where it is shown that the two sets of results are identical. Thus, the primary new results reported here concern the in-plane dynamics of oblate spheroids and triaxial ellipsoids.

3.1.1. *Dynamics of oblate spheroids and triaxial ellipsoids*

As in the case of prolate spheroids (Gao *et al.* 2012), oblate spheroids and triaxial ellipsoids too exhibit trembling and tumbling dynamics. We first discuss the shape dynamics of oblate spheroids. For a given initial aspect ratio $\omega_{1,0} = \omega_{2,0} = \omega_0$, the particle deforms to resemble a thin disk for part of its tumbling/trembling cycle as the elastic capillary number G increases. Since G may be thought of as the inverse of the dimensionless stiffness, increasing G implies increasing deformability. The transition from tumbling to trembling occurs at a critical value of G that depends on ω_0. Figures 4 and 5 show the results for two values of G for $\omega_0 = 2.5$ on either side of the tumbling–trembling transition for an initial orientation of $\theta_0 = \pi/2$ (i.e. the symmetry axis pointing in the velocity gradient direction). It is evident from figure 4(*b*) that the particle tumbles for $G = 0.4$ and trembles for $G = 0.5$.

Figure 5(*a,b*) shows the variations with time of the orientation θ and the angle φ between the x_1 axis and tensile stretch axis. Recall from § 2.1 that the x_1 axis (which characterizes the orientation θ) for an oblate spheroid is the in-plane principal axis of
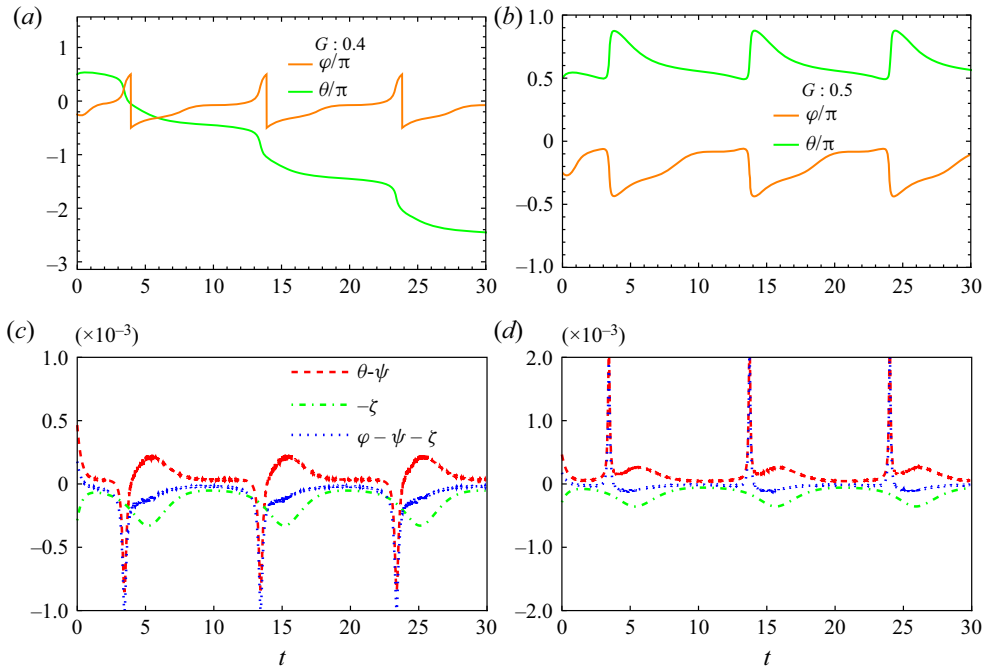
Figure 5. (*a*,*b*) The time variation of the direction of stretch (φ) for the two cases shown in figure 4, namely $G = 0.4$ (*a*) and $G = 0.5$ (*b*). The particle orientation from figure 4(*b*) is superposed. (*c*,*d*) The contributions to the change in orientation due to the vorticity ($-\zeta$) and stretch ($\varphi - \psi$), and the net change ($\varphi - \psi - \zeta$) during each time step corresponding to panels (*a*,*b*). Refer to figure 3 for the definitions of the angles ζ, ϕ and φ. The time step δt is not constant, as it has to be adaptively changed to accurately compute sharp changes.

smaller length. For the stiffer particle ($G = 0.4$), φ changes sign twice during a revolution (figure 5*a*), implying tumbling motion. The transition may be understood by considering the contributions to rotation from stretching and vorticity in every time step δt, shown in figure 5(*c*). We see that, although the orientation change due to stretching $\varphi - \psi$ is positive for part of each cycle, it is smaller in magnitude than the orientation change due to vorticity $-\zeta$; the net change in orientation ($\varphi - \psi) - \zeta$ is therefore always negative, resulting in tumbling. For the softer particle ($G = 0.5$), φ is always negative (figure 5*b*), implying that the x_1 axis lies between the flow direction and the direction of extensional stretch (λ_1); the orientation change due to stretch is therefore always positive (figure 5*d*); it is also larger in magnitude that the orientation change due to vorticity. As a result, the particle trembles – the orientation oscillates about an angle that depends on G and ω_0. The sharp peaks in figure 5(*c*,*d*) correspond to instances when the in-plane aspect ratio (ω_1) is close to unity (figure 4*a*), about which there is rapid variation in φ (figure 5*a*,*b*). The results presented in figures 4 and 5 are for an initial orientation wherein the x_1 axis is aligned with the gradient direction. Any other initial orientation in the plane of shear simply leads to the same dynamics at large time, apart from a short initial transient. Thus, the only signature of the initial orientation is a phase difference in the universal long-time dynamics.

For very stiff particles, such as $G = 0.01$, the orientation of the principal stretch axis exhibits the same qualitative dynamics as that in figure 5(*a*) for $G = 0.4$. The transition from tumbling to trembling (for a fixed ω_0) occurs with increasing G due to the particle deforming into an increasingly anisotropic shape that causes it to spend enough time in orientations where the longer in-plane axis is close to the flow direction and the rate of
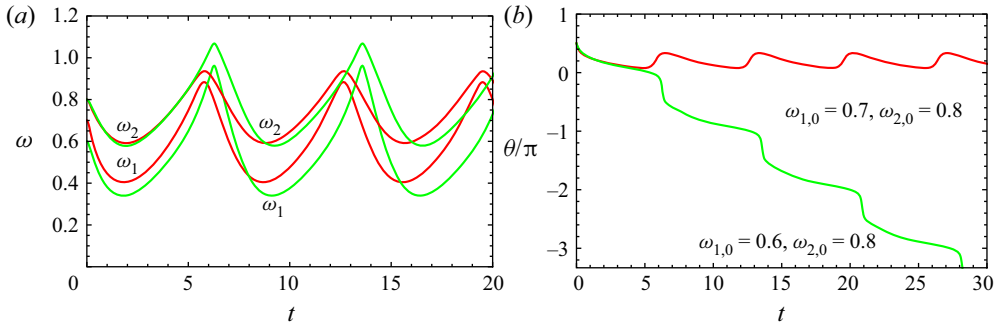
949 A22-14

Figure 6. Dynamics of an initially ellipsoidal elastic particle in the trembling and tumbling regimes at $G = 0.2$. (*a*) In-plane and out-of-plane aspect ratios. (*b*) Orientation of the major axis.

rotation is the lowest, allowing the deformed particle to 'spring back'. It is relevant to contrast the dynamics of elastic and rigid particles ($G = 0$). As there is no stretch dynamics for the latter, they only tumble. Further, a key difference is that while the stress within the elastic particle remains uniform in the limit $G \rightarrow 0$, there is no requirement for the stress to be uniform at $G = 0$; indeed the stress in the latter case is indeterminate. However, we show below that the orientation dynamics of very stiff particles is virtually identical to a rigid one, implying that the stress indeterminacy is not of relevance to the dynamics.

We now come to the shape dynamics of triaxial ellipsoids. Recall from § 2.1 that the x_1 axis in this case is the larger in-plane principal axis in the initial state. Figure 6 displays results for two ellipsoids of different initial aspect ratios with $G = 0.2$, one exhibiting tumbling dynamics and the other trembling. As the stiffness is reduced, there is always a tumbling to trembling transition, no matter what the initial aspect ratios are, which we discuss below. An interesting aspect of elastic triaxial ellipsoids is that the orientation dynamics depends on the initial out-of-plane aspect ratio $\omega_{2,0}$; this is in contrast to rigid ellipsoids, where the dynamics is independent of ω_2, as shown by Jeffery (1922). This difference between rigid and elastic ellipsoids is shown in figure 7; while the orientation dynamics for rigid ellipsoids of different out-of-plane aspect ratios is identical (figure 7*a*), there is a slow down of the tumbling dynamics for elastic particles with decreasing $\omega_{2,0}$, for small G, and a transition from tumbling to trembling with decreasing $\omega_{2,0}$ at the highest G (figure 7*b–d*).

3.1.2. *Phase diagrams of dynamical states for spheroids and triaxial ellipsoids*

As already discussed, for a particle that is initially an oblate spheroid of aspect ratio ω_0, the transition from tumbling to trembling occurs at a critical value of G. Thus, the tumbling–trembling transition can be shown in a G–ω_0 plot, as in the case of prolate spheroids (Gao *et al.* 2012). Figure 8 shows the combined phase diagram for prolate and oblate spheroids. We know from Roscoe (1967) that an initially spherical particle ($\omega_0 = 1$) reaches a steady shape and orientation, regardless of G; this state is represented by the blue vertical line. As the shape deviates from $\omega_0 = 1$ on either side, the particle exhibits a tumbling dynamics for small G and trembling above a critical value of G, which increases as ω_0 progressively deviates from unity on either side. Thus, extreme-aspect-ratio spheroids (slender rods or thin disks) transition to the trembling regime at a large shear rate for a given stiffness. The phase boundary separating the trembling and tumbling regimes is identified at a (G, ω_0) where the dynamics includes an instant of time when the cross-section in the plane of shear is circular ($\omega_1 = 1$).
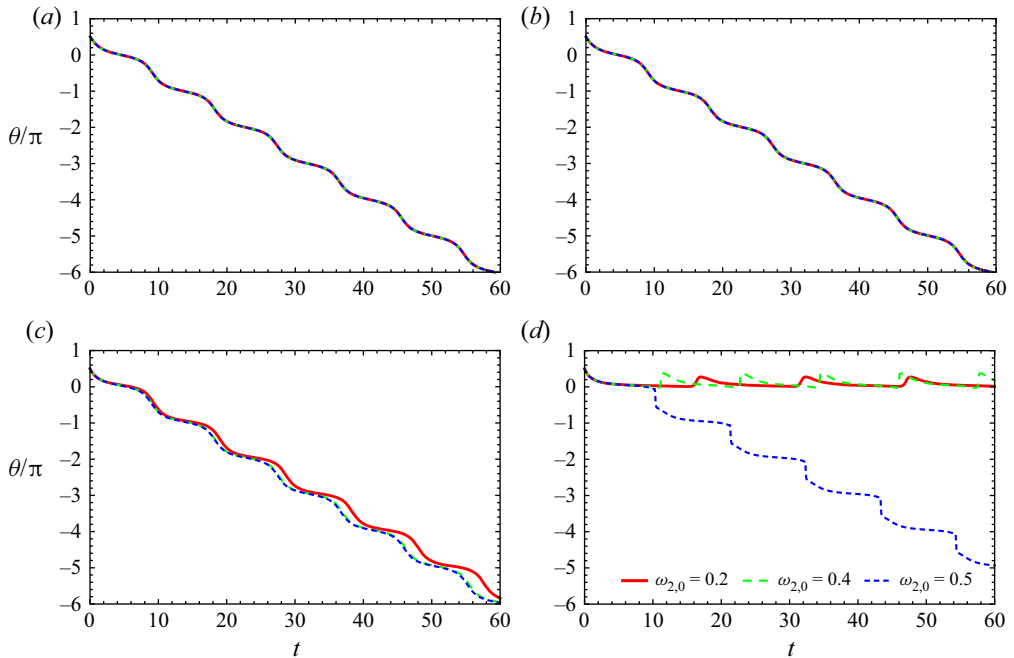
Figure 7. Effect of out-of-plane aspect ratio on the dynamics of an initially ellipsoidal elastic particle with $\omega_{1,0} = 0.4$. (*a*) Perfectly rigid particle ($G = 0$). (*b*) Slightly soft particle with $G = 0.01$. (*c*) Softer particle with $G = 0.1$. (*d*) Soft particle with $G = 0.4$.

The principal axes are interchanged at this instant, resulting in a jump in θ by $\pm\pi/2$; the marginal trajectory on the phase boundary may therefore be regarded as a trembling or tumbling trajectory. Although the trembling–tumbling phase boundaries appear to be symmetric about the $\omega_0 = 1$ axis (suggesting an $\omega_0 \to 1/\omega_0$ equivalence), they are not (see inset of figure 8). This is a departure from the phase diagram for two-dimensional elliptical particles (infinitely long cylinders of elliptical cross-section), where the equations governing the shape dynamics are invariant under the transformation $\omega_0 \to 1/\omega_0$ (Gao *et al.* 2012); indeed, the transformation in the two-dimensional case corresponds trivially to a rotation of the ellipse by $\pi/2$.

For a triaxial ellipsoid in simple shear flow, the phase boundary for the tumbling–trembling transition is a two-dimensional surface in $(\omega_{1,0}, \omega_{2,0}, G)$ space. As accurate resolution of the phase boundary in the three-dimensional parameter space is computationally prohibitive, we only determine, for discrete values of G and $\omega_{2,0}$, the upper and lower bounds of $\omega_{1,0}$ for tumbling and trembling that deviate from the true phase boundary by at most 0.05. They are represented by the light and dark grey surfaces in figure 9(*a*). Thus, for a given set of $(G, \omega_{2,0})$, the lower (light grey) surface represents the lower bound of $\omega_{1,0}$ at which the particle trembles, and the upper (dark grey) surface represents the upper bound of $\omega_{1,0}$ at which it tumbles. Figure 9(*b–d*) shows sections of the phase diagram at fixed values of G, $\omega_{1,0}$ and $\omega_{2,0}$, respectively, so that features of the transition may be seen in greater detail. The vertical edges of the graph in figure 9(*a*) represent the following initial configurations of the particle: a sphere ($\omega_{1,0} = \omega_{2,0} = 1$), a circular disk whose normal is in the vorticity direction ($\omega_{1,0} = 1$, $\omega_{2,0} = 0$), an infinitely slender rod ($\omega_{1,0} = \omega_{2,0} = 0$) in the plane of shear, and a circular disk with its normal in the plane of shear ($\omega_{1,0} = 0$ and $\omega_{2,0} = 1$), respectively. The vertical planes represent
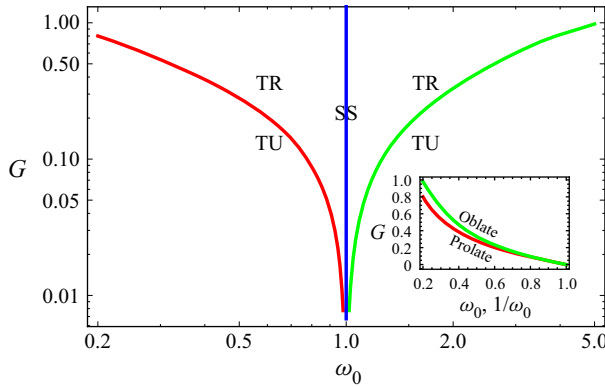
Figure 8. Phase diagram of spheroids in simple shear flow. The types of dynamics exhibited are denoted by the labels SS for steady state, TR for trembling and TU for tumbling.

the following initial configurations: the $\omega_{1,0} = 1$, $\omega_{2,0} < 1$ plane represents an oblate spheroid whose symmetry axis is aligned in the vorticity direction, the $\omega_{1,0} = 0$, $\omega_{2,0} < 1$ plane represents an elliptical disk whose normal is in the plane of shear, the $\omega_{2,0} = 1$, $\omega_{1,0} < 1$ plane represents an oblate spheroid whose symmetry axis is in the plane of shear, and the $\omega_{2,0} = 0$, $\omega_{1,0} < 1$ plane represents an elliptical disk whose normal is along the vorticity axis. Thus, the $\omega_{2,0} = 1$, $\omega_{1,0} < 1$ plane contains the in-plane dynamics of oblate spheroids, and corresponds to the right half of figure 8. Finally, the diagonal vertical plane $\omega_{2,0} = \omega_{1,0}$ represents a prolate spheroid whose symmetry axis is in the plane of shear, and corresponds to the left half of figure 8. We see from figure 9(a) that thin elliptical disks in the plane of shear ($\omega_{2,0} \to 0$) and oblate spheroids whose normal is in the plane of shear ($\omega_{2,0} \to 1$) exhibit a tumbling–trembling transition as G is increased, but thin elliptical disks with normal in the plane of shear ($\omega_{1,0} \to 0$) exhibit either a tumbling or flow-aligning dynamics (see below) for the range of G we have studied. An interesting point to note from figure 9(b,c) is that the tumbling–trembling transition is not significantly influenced by the out-of-plane aspect ratio $\omega_{2,0}$ beyond 0.5; indeed, we find the threshold curve at $\omega_{2,0} = 1$ to be quite close to that for $\omega_{2,0} \to \infty$, which corresponds to elliptical cylinders aligned with the vorticity direction, examined by Gao *et al.* (2012).

Below the lower (light grey) surface in figure 9(a), there are some points represented by the blue circles that denote states where the long axis of the particle does not cross the flow axis. The shape dynamics corresponding to one such point is shown in figure 10, where it is clear that the lengths of the in-plane semi-axes vary as $\alpha_1 \sim t$, $\alpha_2 \sim 1/t$ in the limit $t \to \infty$, and the orientation θ decays to zero as $1/t$. The continuous stretching of the particle along its major axis slows down its rotation, leading to an asymptotic flow-aligning behaviour. For any $G > 0$, there is an interval of small $\omega_{1,0}$ for which the particle extends indefinitely in time and asymptotically aligns with the flow axis. We have not attempted to compute accurately the boundary between such flow-aligning states and the tumbling states, due to the long computation time required. While the flow-aligning state may be physically unrealistic – real elastic particles will undergo plastic deformation beyond a critical stress and eventually rupture – it still is an interesting feature, as it is likely to be present in any continuum elastic model that allows arbitrarily large deformation, and indicates the parameter regime for which particles are likely to rupture. We note that an indefinitely stretching flow-aligning state has also been predicted for an initially
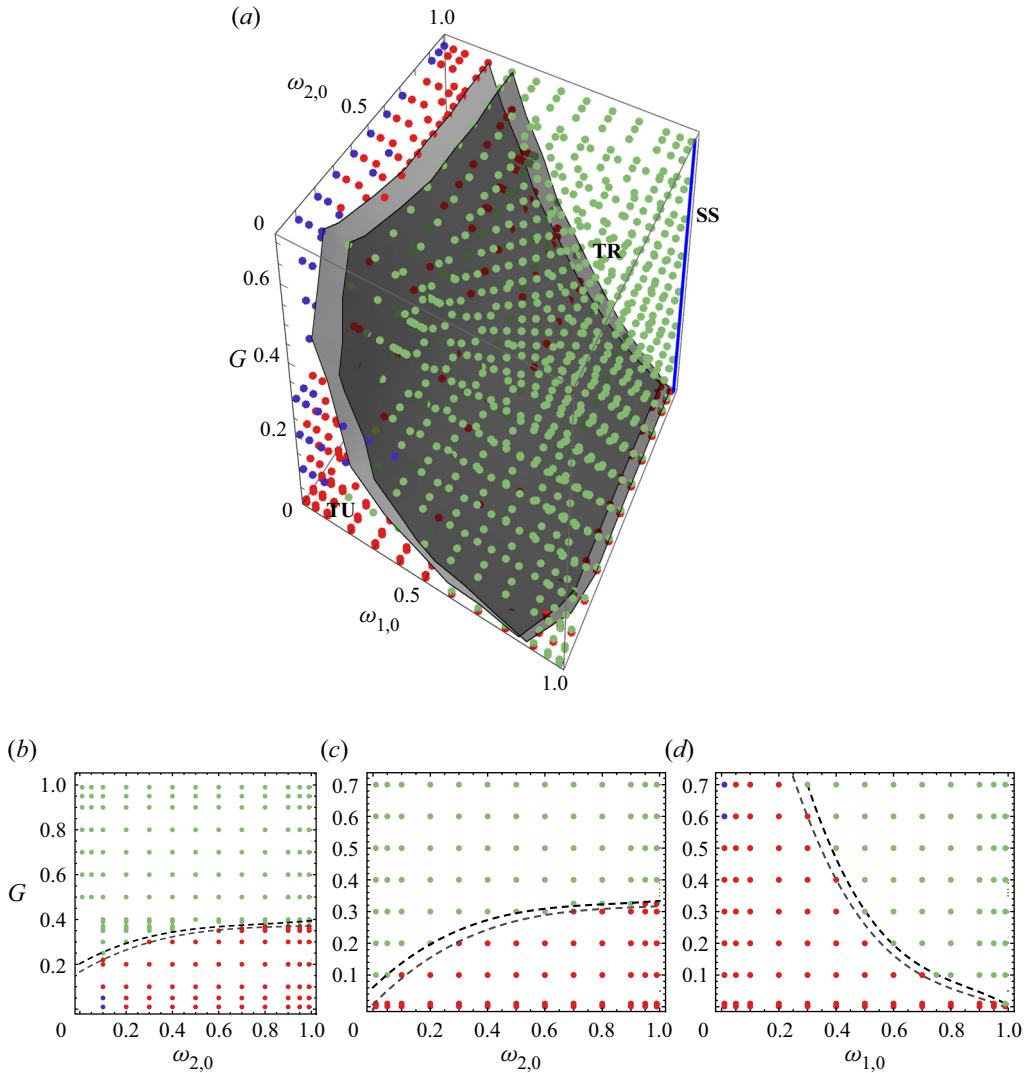
Figure 9. Tumbling–trembling phase diagram of a triaxial ellipsoid in simple shear flow. (*a*) The filled red and green circles represent tumbling (TU) and trembling (TR) dynamical states, respectively. The filled blue circles represent flow-aligning states wherein the long axis of the particle asymptotically approaches the flow axis. The light and dark grey surfaces represent the upper and lower bounds in $\omega_{1,0}$ for tumbling dynamics and trembling dynamics, respectively; the true phase boundary lies between them. (*b–d*) Sections of the phase diagram at (*b*) $G = 0.5$, (*c*) $\omega_{1,0} = 0.5$ and (*d*) $\omega_{2,0} = 0.5$.

spherical liquid drop in a Newtonian fluid subjected to shear above a critical capillary number $Ca \equiv \mu \dot{\gamma} \ell_p / \sigma$ (σ being the interfacial tension) by Wetzel & Tucker (2001). Such an elongated drop will ultimately break up (Barthes-Biesel & Acrivos 1973). There will, however, be differences in the mechanism of breakup between drops and elastic particles, as the Stokes equations governing motion in the former remain valid until breakup, while the neo-Hookean constitutive relation will cease to be valid beyond the point of plastic yield. Further discussion on the similarity and differences in the dynamics of drops, capsules and elastic particles is given in § 4.
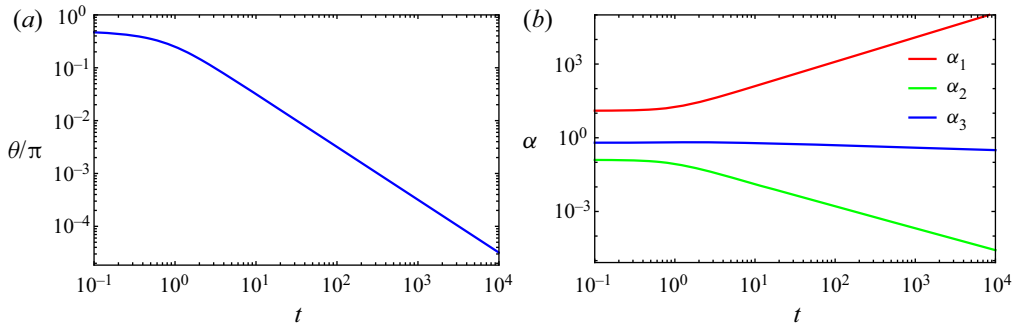
Figure 10. Trajectory of an initial triaxial ellipsoid that asymptotically aligns with the flow direction. The parameter values are $G = 1.0$, $\omega_{1,0} = 0.01$, $\omega_{2,0} = 0.05$. Time variation of (*a*) the orientation and (*b*) lengths of the principal semi-axes α_i.

The rheological responses of dilute suspensions of initially oblate spheroids of aspect ratio $\omega_0 = 2$ and triaxial ellipsoids of aspect ratios $\omega_{1,0} = 0.7$, $\omega_{2,0} = 0.8$ are shown in figure 11. As mentioned in § 2.6, the rheological properties were obtained by averaging over a cycle of the long-time oscillatory response, which is equivalent to averaging over different initial orientations. As G may be thought of as a dimensionless shear rate, it is apparent from figure 11(*a,c*) that the suspension is shear thinning. The reason for this is straightforward to understand: with increasing G, the particle tends to extend and align towards the flow direction, thereby offering less resistance to deformation. The intrinsic shear viscosity $[\mu]_s$ becomes negative for sufficiently large G (which for the cases considered is ~ 1), as found by Gao *et al.* (2011, 2012) for initially spherical and prolate spheroidal particles. This is a result of the extra dissipation in the fluid due to the presence of particles becoming small enough to be more than compensated by the lack of dissipation within the particles. An analogous change in sign of the intrinsic viscosity as a function of the capillary number *Ca* is known for magmas containing highly deformable bubbles (Manga & Loewenberg 2001). Figure 11(*b,d*) shows that the first and second normal stress differences are positive and negative, respectively; as N_1/G and N_2/G are proportional to the corresponding normal stress coefficients, the figure shows mild shear thinning of these coefficients too. A positive N_1 arises from the greater alignment of the longest axis, which is under tension, with the flow direction; a negative N_2 arises from the shortest axis, that is under compression, beginning to align with the gradient direction. The overall response is similar to that of a dilute suspension of rigid spheroids (Brenner 1974).

Our analysis and results consider the particle to be in an initial stress-free state before shear is commenced. We briefly comment on what the dynamics might be if the particle were to have a residual stress in the initial state. The simplest case is when the initial state corresponds to one of the uniformly stressed configurations accessed in the dynamics across any of the steady tank-treading, trembling, tumbling or flow-aligning regimes described above: the dynamics of such an ellipsoid would correspond to that particular configuration, with the only difference being the absence of an initial transient. However, it is unlikely that the dynamics over the entire range of $\omega_{1,0}$, $\omega_{2,0}$ and G covers uniformly stressed ellipsoids of all possible orientations: for example, we do not see a sufficiently slender ellipsoid (that exhibits flow-aligning behaviour in the absence of an initial residual stress) having a finite stress in the compressional quadrant of the simple shear flow arising from a stress-free initial configuration. We may nevertheless make the following plausible speculation: we know that an ellipsoid with a uniform residual stress must relax, in the
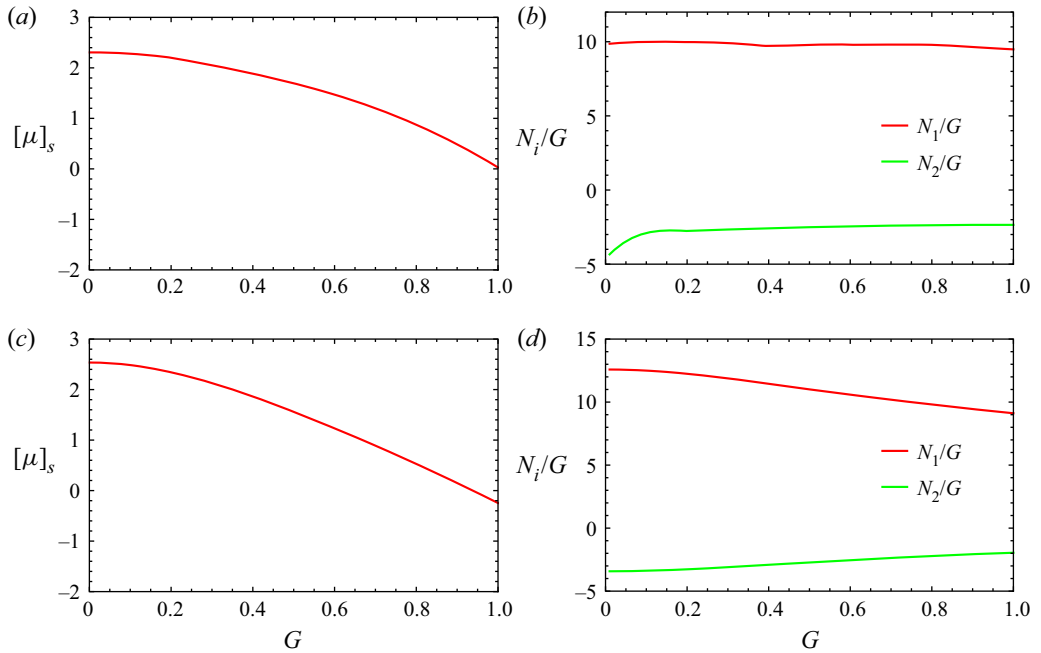
Figure 11. Rheological response of a dilute non-interacting suspension of elastic particles as a function of G. The top row shows the (*a*) intrinsic viscosity and (*b*) normal stress differences for initial oblate spheroids of aspect ratio $\omega_0 = 2$. The bottom row shows the same quantities for initial ellipsoids of aspect ratios $\omega_{1,0} = 0.7$, $\omega_{2,0} = 0.8$.

absence of an imposed shear, to a stress-free state through a sequence of ellipsoidal configurations; this suggests a close relation between the dynamics of such an ellipsoid and the (hypothetical) stress-free ellipsoid that it would relax to. It is then tempting to conclude that these two initial ellipsoidal configurations would converge to the same long-time dynamics, with differences restricted to an initial transient that is similar to initially stress-free configurations with differing orientations converging to the same long-time dynamics (see the discussion in § 2.6). If this were the case, the analysis in the manuscript subsumes the long-time dynamics of initially uniformly stressed ellipsoids. The long-time shape-cum-orientation dynamics of an ellipsoid with a non-uniform residual stress field in the initial state is beyond the scope of the present analysis. However, if the amplitude of the non-uniformity is small, then the shape dynamics would be accessible to a perturbative approach. As this weakly non-uniform residual stress would drive an approach to a marginally non-ellipsoidal stress-free state in the absence of an imposed shear, the analysis of such an initial state is likely to be equivalent to a stability analysis of initially ellipsoidal stress-free configurations to small-amplitude shape perturbations.

3.2. *Effect of particle viscoelasticity*

We now discuss the dynamics of viscoelastic particles in simple shear flow. The shape dynamics of initial spheres and spheroids, and the resulting dilute suspension rheology, are now influenced by G and κ, the ratio of the viscosity of the particle to that of the suspending fluid. As already discussed, an initially spherical elastic particle ($\kappa = 0$) attains a steady ellipsoidal shape with its longest axis orientated between the extensional and flow directions. For non-zero κ, an initial spherical particle exhibits a damped oscillatory
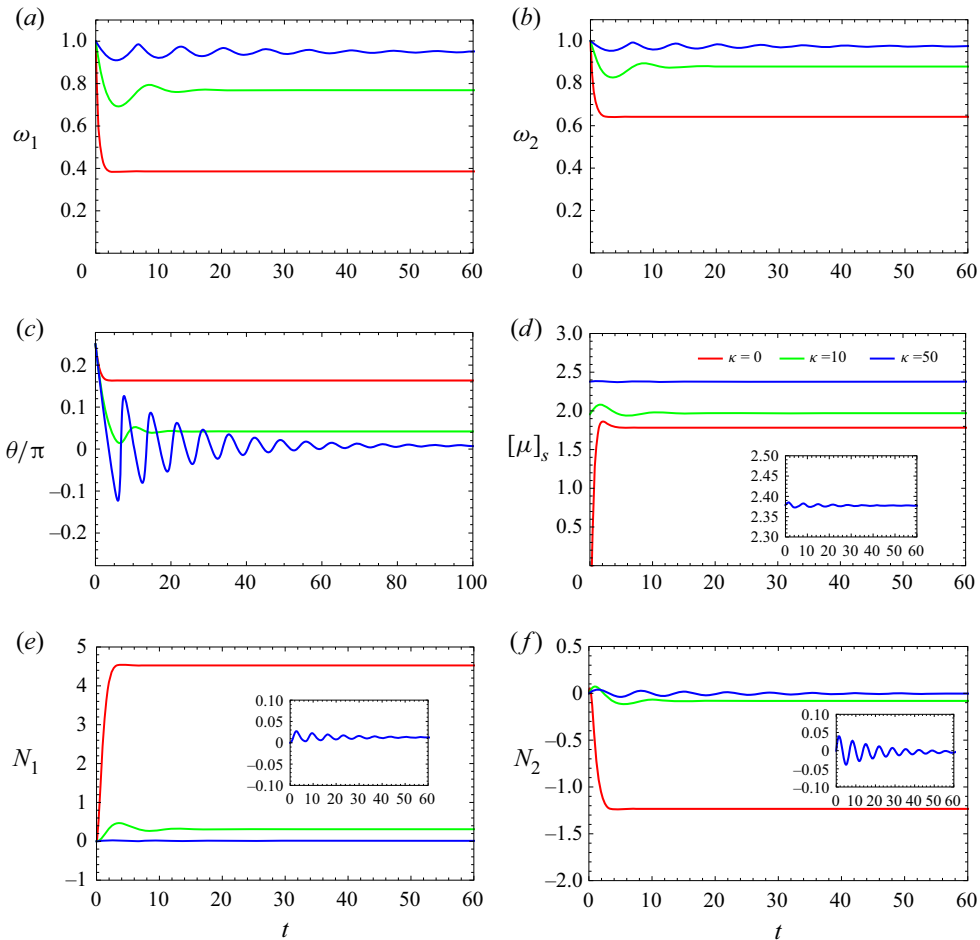
Figure 12. Effect of the viscosity ratio κ on the dynamics of an initially spherical viscoelastic particle for $G = 0.4$. (*a*) Particle orientation. (*b*) In-plane aspect ratio. (*c*) Out-of-plane aspect ratio. (*d*) Intrinsic viscosity. (*e*) First normal stress difference and (*f*) second normal stress difference.

approach to the eventual steady state, with the amplitude of the oscillations increasing with κ to begin with (compare $\kappa = 0$ and 10 in figure 12). However, in the limit $\kappa \to \infty$, the dynamics must approach that of a rigid sphere. This implies that the amplitude of shape oscillations must eventually decrease with increasing κ (compare $\kappa = 10$ and 50 in figure 12). Further, since a rigid sphere rotates with a uniform angular velocity (equalling half the ambient vorticity), the orientation dynamics must transition to a tumbling behaviour for sufficiently large κ, with θ continuously decreasing with time (not shown). In figure 12(*d*), the intrinsic shear viscosity increases with κ until it reaches 2.5, the Einstein coefficient for the limit $\kappa \to \infty$. On the other hand, the magnitudes of the first and second normal stress differences decrease with increasing κ (figure 12*e*,*f*); they understandably tend to zero in the limit $\kappa \to \infty$, as in a dilute suspension non-interacting rigid particles is Newtonian.

It is useful to consider the analogy between the dynamics of the initially spherical viscoelastic particle, discussed above, and that of a drop with interfacial tension; the elasticity in the latter case is characterized by *Ca*. It is known from the work of
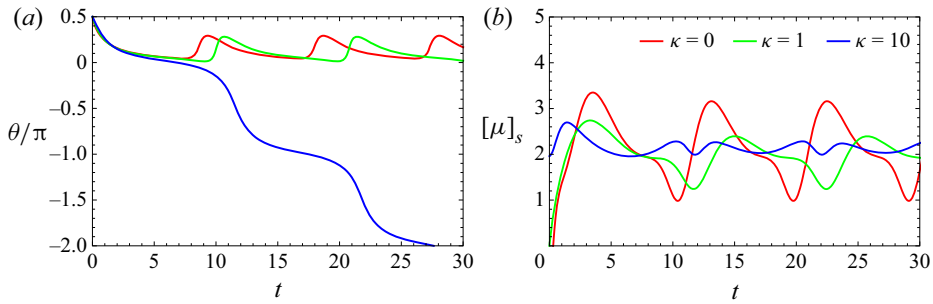
Figure 13. Effect of the viscosity ratio κ on the dynamics of a viscoelastic particle whose initial shape is a prolate spheroid ($\omega_0 = 0.5$) for $G = 0.4$. (*a*) Particle orientation and (*b*) intrinsic viscosity.

Cox (1969) that the dynamics of a drop in simple shear flow, for $Ca \ll 1$, changes qualitatively with increasing κCa. For small κCa, the initially spherical drop exhibits an overdamped approach to a steady ellipsoidal shape whose longest axis is approximately aligned with the extensional axis of the ambient simple shear. With increasing κCa, the approach to the deformed steady shape transitions to an underdamped one, with the time scale of the damped oscillatory behaviour eventually diverging as $O(\kappa Ca)$ for $\kappa Ca \gg 1$; the deformed drop is now nearly aligned with the flow direction at steady state. For the viscoelastic particle, we expect κG to play a role analogous to κCa for the drop. However, a key difference, illustrated in figure 12, is that the transition from overdamped to underdamped oscillations upon increasing κG is not restricted to small values of G. From the insets of figure 12(*d–f*), the time scale characterizing the damping of the oscillations is seen to clearly increase with increasing κ, consistent with the aforementioned drop analogy; the eventual steady shape also aligns more closely with the flow direction. Note that the time period of the oscillations, for both the particle and the drop, remains finite, and of order the inverse shear rate, for large κ.

As already seen, an initially prolate spheroidal elastic particle exhibits a periodic oscillatory dynamics after a short initial transient. A typical result for a viscoelastic prolate spheroid is shown in figure 13, where we observe a dependence of the nature of the dynamics on κ: the purely elastic particle ($\kappa = 0$) exhibits trembling, but it changes to tumbling as κ is increased. Thus, the particle viscosity tends to shift the trembling–tumbling phase boundary upwards in figure 8. This is not surprising in light of the fact that a rigid spheroid ($\kappa = \infty$) must exhibit a tumbling dynamics. We did not observe damping of the oscillations for the range of parameter space we explored, but it is reasonable to expect damped oscillations that settle at large time to periodic oscillations of constant amplitude (corresponding to tumbling or trembling) as ω_0 approaches unity. The variation of the intrinsic viscosity with time is shown for different κ in figure 13(*b*). The viscosity variation over a cycle is greater for the trembling particle ($\kappa = 0$) than the tumbling ones ($\kappa = 1, 10$) owing to the amplitude of shape variation decreasing with increasing κ.

4. Summary and conclusions

We have described a method to determine the shape dynamics of elastic and viscoelastic particles whose initial (stress-free) shape is ellipsoidal, suspended in a Newtonian fluid subjected to a simple shear. The particle is allowed to undergo an arbitrarily large deformation, with the elastic stress being governed by the neo-Hookean

949 A22-22

constitutive model. We determine the stress in the particle by extending the method of Roscoe (1967) to dynamically evolving states. Our method is conceptually and analytically simpler than the stress polarization technique of Gao *et al.* (2011), and importantly, also applicable to any constitutive model for the elastic stress.

For initially spherical elastic particles we recover the steady shape and orientation derived by Roscoe (1967); for initially prolate spheroids we recover the trembling and tumbling dynamics shown by Gao *et al.* (2012). We find that initial oblate spheroids and triaxial ellipsoids also exhibit tumbling and trembling dynamics, and have computed the tumbling–trembling phase diagram in the G–aspect ratio parameter space, where G is the elastic capillary number (inverse of the dimensionless stiffness); unlike their rigid counterparts, the dynamics of elastic triaxial ellipsoids depends on the out-of-plane aspect ratio. In addition to the steady, tumbling and trembling dynamical states, we have found the existence of a novel flow-aligning state, in which the particle extends indefinitely and asymptotically aligns with the flow direction. For given initial aspect ratios ($\omega_{1,0}, \omega_{2,0}$), an ellipsoid exhibits a trembling dynamics above a critical value of the elastic capillary number G, and a tumbling dynamics below this critical value. Flow-aligning states are only seen when $\omega_{1,0}$ is sufficiently small. While such states must transition to tumbling beyond a threshold $\omega_{1,0}$, for a fixed G, we have not accurately determined this boundary between the flow-aligning and the tumbling states due to limitations in computation time. Initially spherical viscoelastic particles in simple shear flow exhibit damped oscillations as they approach a steady shape, provided the ratio of particle to fluid viscosity κ is sufficiently large. For initial prolate spheroids, increasing κ expands the tumbling regime in the G–ω_0 plane.

We have obtained the rheological properties for a dilute suspension of non-interacting randomly oriented elastic particles, of a given ellipsoidal shape, by averaging over the shape dynamics corresponding to all initial orientations. The intrinsic shear viscosity exhibits shear thinning, and is negative for sufficiently large G, implying that the suspension has a lower viscosity than the suspending fluid. The first normal stress difference is found to be positive, and the second normal stress is negative and much smaller in magnitude, as for dilute suspensions of rigid spheroids.

Our results are amenable to experimental verification using polymer gel particles, where one can tune the stiffness by controlling the degree of cross-linking. We have focused on the in-plane dynamics of ellipsoidal elastic particles in this paper, but the shape-cum-orientation dynamics of particles starting from out-of-plane orientations is also of interest – we plan to address this in a later paper. Earlier studies on capsules (Dupont, Salsac & Barthes-Biesel 2013) and vesicles (Zhao & Shaqfeh 2011) suggest that the off-plane dynamics can differ qualitatively from those of rigid ellipsoids.

A comparison of our results for elastic particles in an ambient shear flow with those reported earlier for drops, capsules and vesicles is in order. As discussed in § 3.1.2, drops too exhibit a transition to an indefinitely stretching flow-aligning state above a critical capillary number. The key difference is that the initial stress-free state can only be spherical for drops with finite interfacial tension, while it can be ellipsoidal for elastic particles. However, a more detailed analogy can be made if we consider the limit of zero interfacial tension. Although interfacial tension is unavoidable between dissimilar liquids, this limit is useful to consider as drops may assume initial non-spherical shapes. Moreover, it is a useful limit for considering the case of $Ca \gg 1$ at time scales of $O(\dot{\gamma}^{-1})$, as weak interfacial forces become important only at longer time (Jackson & Tucker 2003). Wetzel & Tucker (2001) found that an initially ellipsoidal drop of a given (sufficiently large) viscosity ratio exhibits steady flow-aligned tank treading at a critical value of the

initial in-plane aspect ratio $(\omega_{1,0} = \omega_c < 1)$. As $\omega_{1,0}$ is decreased from ω_c, there is a transition to trembling, and then to tumbling; there are similar transitions to trembling and tumbling when $\omega_{1,0}$ is increased from ω_c. These transition sequences are analogous to the ones we see for prolate and oblate spheroidal elastic particles, respectively, for a fixed G and varying $\omega_{1,0}$, but with the differences that the tank-treading steady state for an elastic particle is achieved only for an initial sphere, and it is not oriented along with the flow direction. Moreover, for drops in the absence of interfacial tension, the reversibility constraints associated with the Stokes equations imply that there can be no transient dynamics preceding the steady flow-aligned tank-treading state; for elastic particles, the combination of elastic and viscous forces allow for a transient evolution to the steady state.

Spheroidal elastic capsules (liquid drops enclosed by an elastic membrane) also exhibit steady tank-treading, trembling and tumbling regimes, depending on the initial aspect ratio, viscosity ratio and the capillary number (defined based on the membrane elastic modulus) (Walter, Salsac & Barthes-Biesel 2011). Red blood cells, which are capsules whose membrane is elastic and area preserving, also exhibit steady tank-treading, tumbling and trembling shape dynamics, but not the indefinitely stretching flow-aligned state owing to the large energy cost associated with any change in the membrane area. Moreover, for a fixed excess area (that quantifies the departure from spherical shape in the stress-free state) there is a transition from tumbling to trembling to steady tank treading as the capillary number increases. A notable point is that the relatively complex biconcave equilibrium shape of red blood cells can result in a steady tank-treading state, owing to the combination of the bending elasticity and the constraint of constant area of the membrane (Vlahovska, Podgorski & Misbah 2009).

We conclude with some remarks on the potential applications of our study. Soft particle suspensions are widely encountered in living systems, blood being a prominent example. While red blood cells have only an elastic membrane and are highly deformable, most other blood cells have a cytoskeleton that imparts elasticity to the cell body. Cancer cells are significantly stiffer than normal cells, which is thought to aid their margination to the walls of blood vessels, thereby leading to metastasis (Fedosov & Gompper 2014; Czaja *et al.* 2020). Suspensions of elastic and viscoelastic particles are also widely encountered in large-scale industrial fermentation processes, such as brewing of alcoholic beverages using suspensions of yeast cells. A relatively recent technology is mammalian cell culture for the production of drugs and vaccines, where it has been found to be beneficial to grow the cells on elastic hydrogels particles (Wei *et al.* 2020). All these systems are without doubt much more complex than the simple problems we have considered: the cytoskeleton in living cells is active, and yeast cells typically form agglomerates in fermentation tanks. Nevertheless, the rheology and dynamics (such as segregation and margination) of these suspensions is important in some stages of their processing. This paper is a first step in our effort to understand the rheology and dynamics of suspensions of elastic and viscoelastic particles. The assumption of uniform deformation in the particles also limits the utility of our results to uniformly dispersed dilute suspensions, but in the forthcoming paper we consider interactions between elastic particles in close proximity, which will be useful in understanding the rheology of dense suspensions.

Declaration of interests. The authors report no conflict of interest.

Author ORCIDs.

Ⓘ Ganesh Subramanian https://orcid.org/0000-0003-4314-3602;

Ⓘ Prabhu R. Nott https://orcid.org/0000-0003-0656-2648.

Appendix A. Expressions for g_i, g_i' and g_i''

The quantities g_i, g_i' and g_i'' that appear in § 2.1 in the expression for the deviatoric stress in the fluid $\boldsymbol{A}'$ are elliptic integrals that depend on the semi-axis lengths α_i. They were given by Jeffery (1922), and reproduced in the notation used in this paper by Roscoe (1967). The expressions for g_1, g_1' and g_1'' are

$$g_1 = \int_0^\infty \frac{d\lambda}{(\alpha_1^2 + \lambda)\Delta}, \tag{A1a}$$

$$g_1' = \int_0^\infty \frac{d\lambda}{(\alpha_2^2 + \lambda)(\alpha_3^2 + \lambda)\Delta}, \tag{A1b}$$

$$g_1'' = \int_0^\infty \frac{\lambda d\lambda}{(\alpha_2^2 + \lambda)(\alpha_3^2 + \lambda)\Delta}, \tag{A1c}$$

where $\Delta = [(\alpha_1^2 + \lambda)(\alpha_2^2 + \lambda)(\alpha_3^2 + \lambda)]^{1/2}$. Expressions for g_2, g_3, g_2', g_3', g_2'' and g_3'' are obtained by cyclic permutation of indices in (A1).

Appendix B. Particle strain rate and vorticity fields

Here, we provide the final expressions for the strain rate and vorticity fields inside the particle obtained by solving the equations derived from the continuity of the traction on the particle surface.

B.1. *Elastic particles*

The diagonal components of the strain rate and vorticity fields inside an elastic particle can be obtained by solving (2.8a,b). They are expressed in the following quotient form for convenience:

$$D_{11}^p = \frac{P_{11}^p}{Q_{11}^p}, \quad D_{22}^p = \frac{P_{22}^p}{Q_{22}^p}, \tag{B1a,b}$$

where

$$
\begin{aligned}
P_{11}^p &= (4\sigma_{11}^p - 2(\sigma_{22}^p + \sigma_{33}^p) + 5(2D_{22}^\infty(I_{12} - I_{23} - J_{12} + J_{23}) \\
&\quad + D_{11}^\infty(-2I_{23} - J_{12}(4 + 5J_{12}) + I_{12}(-4 + 5I_{12} + 10I_{23} - 10J_{23}) + 2J_{23}) \\
&\quad - (I_{12} + I_{23} - J_{12} - J_{23})\sigma_{11}^p + (I_{23} - J_{23})\sigma_{22}^p + (I_{12} - J_{12})\sigma_{33}^p)),
\end{aligned} \tag{B2a}
$$

$$
\begin{aligned}
P_{22}^p &= (10D_{11}^\infty(I_{12} - I_{23} + J_{12} + J_{23}) + 5(D_{22}^\infty(-2I_{23} + (4 - 5J_{12})J_{12} \\
&\quad + I_{12}(-4 + 5I_{12} + 10I_{23} - 10J_{23}) + 2J_{23}) + I_{23}(\sigma_{11}^p - \sigma_{22}^p) \\
&\quad + J_{23}(-\sigma_{11}^p + \sigma_{22}^p) - (I_{12} + J_{12})(\sigma_{22}^p - \sigma_{33}^p)) - 2(\sigma_{11}^p - 2\sigma_{22}^p + \sigma_{33}^p)),
\end{aligned} \tag{B2b}
$$

$$Q_{11}^p = Q_{22}^p = (12 - 20I_{23} - 25J_{12}^2 + 5I_{12}(-8 + 5I_{12} + 10I_{23} - 10J_{23}) + 20J_{23}). \tag{B2c}$$

Here, σ_{ij}^p are the components of the elastic particle stress, D_{ij}^∞ are the strain rate components of the externally imposed flow and I_{ij} and J_{ij} are functions of the shape of

the particle, defined in (2.9). The incompressibility constraint on the particle provides the relation $D_{33}^p = -(D_{11}^p + D_{22}^p)$.

The expressions for the shear components of the strain rate and vorticity fields inside the particle can be obtained by solving (2.13) and (2.14). They can be expressed in quotient form as

$$D_{12}^p = \frac{P_{12}^p}{Q_{12}^p}, \tag{B3}$$

where

$$P_{12}^p = (-4D_{12}'(g_3'\alpha_2^2(\alpha_1^2 - \alpha_2^2) + g_1(\alpha_1^2 + \alpha_2^2)) + g_3'(\alpha_1^2 + \alpha_2^2)(g_1\alpha_1^2 + g_2\alpha_2^2)\sigma_{12}^p), \tag{B4a}$$

$$Q_{12}^p = (2((-2 + g_2)g_3'\alpha_1^2\alpha_2^2 + (2 + g_2)g_3'\alpha_2^4 + g_1(-2 + g_3'\alpha_1^2)(\alpha_1^2 + \alpha_2^2))), \tag{B4b}$$

and

$$W_{12}^p = W_{12}' - \left(\frac{\alpha_1^2 - \alpha_2^2}{\alpha_1^2 + \alpha_2^2}\right)(D_{12}^\infty - D_{12}^p). \tag{B5}$$

The α_i values are the lengths of the semi-axes of the particle and g_i and g_i' are functions of α_i, defined in Appendix A. Expressions for D_{23}^p, D_{13}^p, W_{23}^p and W_{13}^p are obtained by cyclic permutation of the indices in (B3) and (B5).

B.2. *Viscoelastic particles*

In a similar manner, the components of the strain rate and vorticity fields of a viscoelastic particle can be obtained by solving (2.30). For convenience, they are expressed in the following quotient forms:

$$D_{11}^p = \frac{P_{11}^p}{Q_{11}^p}, \quad D_{22}^p = \frac{P_{22}^p}{Q_{22}^p}, \quad D_{12}^p = \frac{P_{12}^p}{Q_{12}^p}, \tag{B6a–c}$$

where

$$\begin{aligned}P_{11}^p = &((-6 + 5I_{12} + 10I_{23} - 5J_{12} - 10J_{23} + 6\kappa)(5D_{22}^\infty(-I_{12} + J_{12}) + 5D_{11}^\infty(I_{12} + J_{12})\\ &- \sigma_{11}^e + \sigma_{22}^e) + (-2 + 5I_{12} - 5J_{12} + 2\kappa)(5D_{22}^\infty(I_{12} + 2I_{23} - J_{12} - 2J_{23})\\ &+ 5D_{11}^\infty(I_{12} + 2I_{23} + J_{12} - 2J_{23}) - \sigma_{11}^e - \sigma_{22}^e + 2\sigma_{33}^e)),\end{aligned} \tag{B7a}$$

$$\begin{aligned}P_{22}^p = &(-10D_{11}^\infty(I_{12} - I_{23} + J_{12} + J_{23})(\kappa - 1) + 5D_{22}^\infty(-2I_{23} + (4 - 5J_{12})J_{12}\\ &+ I_{12}(-4 + 5I_{12} + 10I_{23} - 10J_{23}) + 2J_{23} + 2\kappa(2I_{12} + I_{23} - 2J_{12} - J_{23}))\\ &+ (-2 + 5I_{23} - 5J_{23} + 2\kappa)\sigma_{11}^e + (4 - 5I_{12} - 5I_{23} - 5J_{12} + 5J_{23} - 4\kappa)\sigma_{22}^e\\ &+ (-2 + 5I_{12} + 5J_{12} + 2\kappa)\sigma_{33}^e),\end{aligned} \tag{B7b}$$

$$\begin{aligned}Q_{11} = 2Q_{22}, \quad Q_{22}^p = &(25I_{12}^2 - 25J_{12}^2 - 4(3 - 5I_{23} + 5J_{23} - 3\kappa)(\kappa - 1)\\ &+ 10I_{12}(-4 + 5I_{23} - 5J_{23} + 4\kappa)),\end{aligned} \tag{B7c}$$

$$\begin{aligned}P_{12}^p = &(-8g_1D_{12}^\infty + ((8\,g_3'D_{12}^\infty\alpha_2^2(-\alpha_1^2 + \alpha_2^2))/(\alpha_1^2 + \alpha_2^2))\\ &+ 2\,g_3'(g_1\alpha_1^2 + g_2\alpha_2^2)\sigma_{12}^e),\end{aligned} \tag{B7d}$$

$$Q_{12}^p = (-8g_1 + ((8\,g_3'\alpha_2^2(-\alpha_1^2 + \alpha_2^2))/(\alpha_1^2 + \alpha_2^2)) - 4\,g_3'(\kappa - 1)(g_1\alpha_1^2 + g_2\alpha_2^2)), \tag{B7e}$$
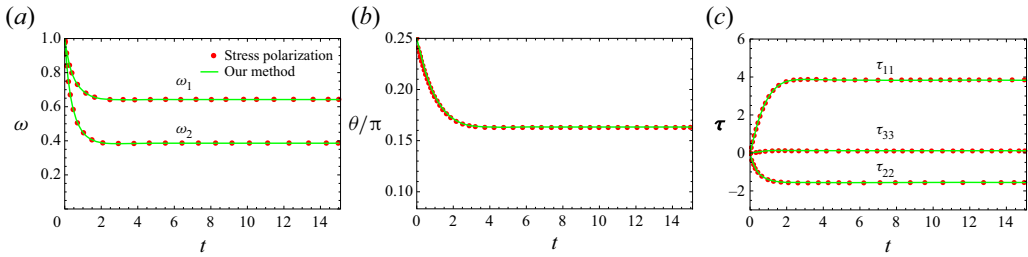
949 A22-26

Figure 14. Transient response of an initial spherical particle at $G = 0.4$. (*a*) In-plane and out-of-plane aspect ratios. (*b*) Particle major axis orientation. (*c*) Particle principal stress components. The shear component of stress remains zero independent of time.
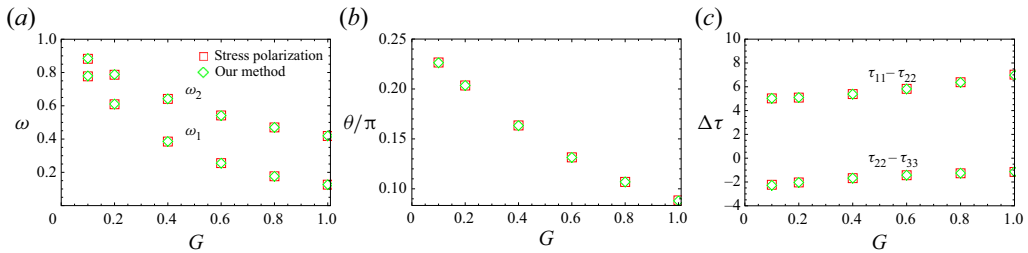

Figure 15. Steady state properties of an initial spherical particle as a function of G. (*a*) In-plane and out-of-plane aspect ratios. (*b*) Particle major axis orientation. (*c*) Normal stress component differences, $N_1 \equiv \tau_{11} - \tau_{22}$ and $N_2 \equiv \tau_{22} - \tau_{33}$.

and

$$W_{12}^p = W_{12}^\infty - \left(\frac{\alpha_1^2 - \alpha_2^2}{\alpha_1^2 + \alpha_2^2} \right) (D_{12}^\infty - D_{12}^p). \tag{B8}$$

Expressions for D_{23}^p, D_{13}^p, W_{23}^p and W_{13}^p are obtained by cyclic permutation of the indices in (B6*a*–*c*) and (B8).

Appendix C. Validation of our method

As noted in § 3.1, we validated our method for computing the shape dynamics of elastic particles by comparing with the results obtained from the stress polarization technique of Gao *et al.* (2011, 2012) for elastic particles that are initially spherical or prolate spheroidal in shape. The results for stress polarization technique were computed by us.

C.1. *Elastic sphere in shear flow*

The transient dynamics of an initially spherical particle for $G = 0.4$ in shear flow is shown in figure 14, where the particle reaches a steady shape and orientation in a dimensionless time of $O(1)$. The shape, orientation and stress in the particle at steady state as a function of G are shown in figure 15. At steady state the particle is a prolate spheroid whose major axis is in the plane of shear, oriented between the flow and tensile directions of the imposed flow, i.e. at $0 < \theta < \pi/4$. It is clear that the two methods yield identical results.
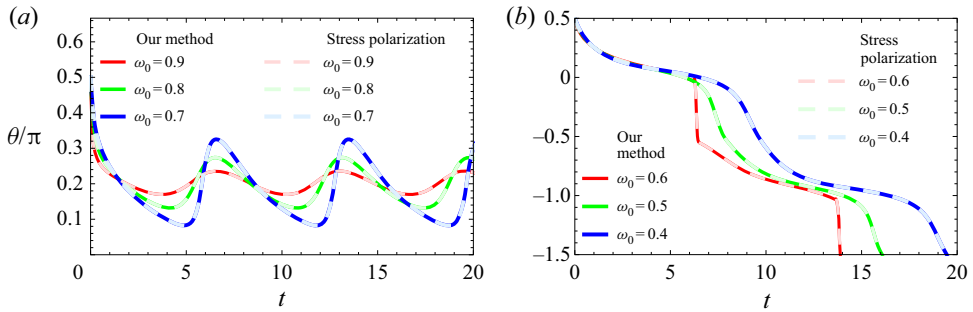
949 A22-27

Figure 16. Orientation dynamics of an initial prolate spheroidal particle at $G = 0.2$. (*a*) Trembling and (*b*) tumbling regimes.
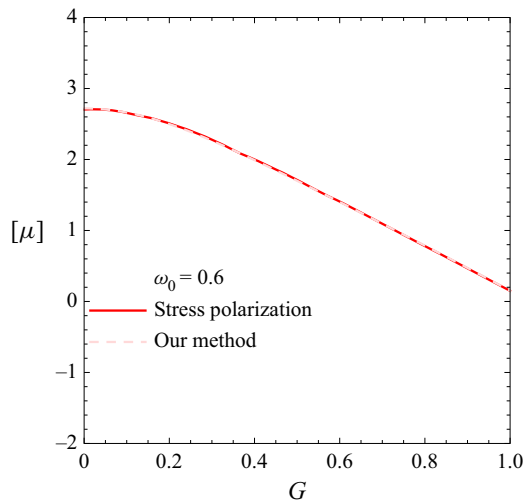

Figure 17. Intrinsic viscosity of a suspension initially prolate spheroids ($\omega_0 = 0.6$) as a function of G. The viscosity is averaged over a tumbling or trembling cycle. The stress polarization data are taken from Gao *et al.* (2012).

C.2. *Elastic prolate spheroid in shear flow*

The dynamics of a prolate spheroidal particle at $G = 0.2$. Figure 16 shows results for a range of initial aspect ratio ω_0; the dynamics corresponds to trembling for $1 > \omega_0 \geq 0.7$ (figure 16*a*), and tumbling for $\omega_0 \leq 0.6$ (figure 16*b*). The trembling–tumbling transition is close to $\omega_0 = 0.6$, for which a sharp change in the orientation by $\pi/2$ is seen. The phase diagram for prolate spheroids shown in figure 8 is in exact agreement with the same obtained by Gao *et al.* (2012) using the stress polarization technique.

C.3. *Intrinsic viscosity*

The intrinsic viscosity of a dilute suspension of initially prolate spheroids of aspect ratio $\omega_0 = 0.6$ (which exhibit a tumbling dynamics) as a function of the elastic capillary number G is shown in figure 17. The intrinsic viscosity is averaged over a tumbling cycle to represent the mean rheological property of a dilute suspension. Here again, we find that the results of our method are in exact agreement with the data of Gao *et al.* (2012).

REFERENCES

BARTHES-BIESEL, D. & ACRIVOS, A. 1973 Deformation and burst of a liquid droplet freely suspended in a linear shear field. *J. Fluid Mech.* **61**, 1–21.

BATCHELOR, G.K. & GREEN, J.T. 1972 The determination of the bulk stress in a suspension of spherical particles to order c^2. *J. Fluid Mech.* **56** (3), 401–427.

BOSSIS, G. & BRADY, J.F. 1984 Dynamic simulation of sheared suspensions. I. General method. *J. Chem. Phys.* **80** (10), 5141–5154.

BRENNER, H. 1974 Rheology of a dilute suspension of axisymmetric Brownian particles. *Intl J. Multiphase Flow* **1** (2), 195–341.

BUTLER, J.E. & SNOOK, B. 2018 Microstructural dynamics and rheology of suspensions of rigid fibers. *Annu. Rev. Fluid Mech.* **50**, 299–318.

CERF, R. 1952 On the frequency dependence of the viscosity of high polymer solutions. *J. Chem. Phys.* **20** (3), 395–402.

COX, R.G. 1969 The deformation of a drop in a general time-dependent fluid flow. *J. Fluid Mech.* **37** (3), 601–623.

CZAJA, B., GUTIERREZ, M., ZÁVODSZKY, G., DE KANTER, D., HOEKSTRA, A. & ENIOLA-ADEFESO, O. 2020 The influence of red blood cell deformability on hematocrit profiles and platelet margination. *PLoS Comput. Biol.* **16** (3), e1007716.

DABADE, V., MARATH, N.K. & SUBRAMANIAN, G. 2016 The effect of inertia on the orientation dynamics of anisotropic particles in simple shear flow. *J. Fluid Mech.* **791**, 631–703.

DANKER, G., BIBEN, T., PODGORSKI, T., VERDIER, C. & MISBAH, C. 2007 Dynamics and rheology of a dilute suspension of vesicles: higher-order theory. *Phys. Rev.* E **76** (4), 041905.

DANKER, G. & MISBAH, C. 2007 Rheology of a dilute suspension of vesicles. *Phys. Rev. Lett.* **98** (8), 088104.

DUPONT, C., SALSAC, A.-V. & BARTHES-BIESEL, D. 2013 Off-plane motion of a prolate capsule in shear flow. *J. Fluid Mech.* **721**, 180–198.

EINSTEIN, A. 1906 Eine neue bestimmung der moleküldimensionen. *Ann. Phys.* **324** (2), 289–306.

ESHELBY, J.D. 1957 The determination of the elastic field of an ellipsoidal inclusion, and related problems. *Proc. R. Soc. Lond.* A **241** (1226), 376–396.

ESHELBY, J.D. 1959 The elastic field outside an ellipsoidal inclusion. *Proc. R. Soc. Lond.* A **252** (1271), 561–569.

FEDOSOV, D.A. & GOMPPER, G. 2014 White blood cell margination in microcirculation. *Soft Matt.* **10** (17), 2961–2970.

FRÖHLICH, A. & SACK, R. 1946 Theory of the rheological properties of dispersions. *Proc. R. Soc. Lond.* A **185** (1003), 415–430.

GALLIER, S., LEMAIRE, E., LOBRY, L. & PETERS, F. 2014 A fictitious domain approach for the simulation of dense suspensions. *J. Comput. Phys.* **256**, 367–387.

GAO, T. & HU, H.H. 2009 Deformation of elastic particles in viscous shear flow. *J. Comput. Phys.* **228** (6), 2132–2151.

GAO, T., HU, H.H. & CASTAÑEDA, P.P. 2011 Rheology of a suspension of elastic particles in a viscous shear flow. *J. Fluid Mech.* **687**, 209–237.

GAO, T., HU, H.H. & CASTANEDA, P.P. 2012 Shape dynamics and rheology of soft elastic particles in a shear flow. *Phys. Rev. Lett.* **108** (5), 058302.

GODDARD, J.D. & MILLER, C. 1967 Nonlinear effects in the rheology of dilute suspensions. *J. Fluid Mech.* **28** (4), 657–673.

GUEDDA, M., BENLAHSEN, M. & MISBAH, C. 2014 Rheological properties of a vesicle suspension. *Phys. Rev.* E **90** (5), 052302.

JACKSON, N.E. & TUCKER, C.L. 2003 A model for large deformation of an ellipsoidal droplet with interfacial tension. *J. Rheol.* **47** (3), 659–682.

JEFFERY, G.B. 1922 The motion of ellipsoidal particles immersed in a viscous fluid. *Proc. R. Soc. Lond.* A **102** (715), 161–179.

KANTSLER, V. & STEINBERG, V. 2006 Transition to tumbling and two regimes of tumbling motion of a vesicle in shear flow. *Phys. Rev. Lett.* **96** (3), 036001.

KRAUS, M., WINTZ, W., SEIFERT, U. & LIPOWSKY, R. 1996 Fluid vesicles in shear flow. *Phys. Rev. Lett.* **77** (17), 3685.

KRIEGER, I.M. 1972 Rheology of monodisperse latices. *Adv. Colloid Interface Sci.* **3** (2), 111–136.

DE KRUIF, C.G., VAN IERSEL, E.M.F., VRIJ, A. & RUSSEL, W.B. 1985 Hard sphere colloidal dispersions: viscosity as a function of shear rate and volume fraction. *J. Chem. Phys.* **83** (9), 4717–4725.

LADD, A.J.C. 1994 Numerical simulations of particulate suspensions via a discretized Boltzmann equation. Part 1. Theoretical foundation. *J. Fluid Mech.* **271**, 285–309.

MANGA, M. & LOEWENBERG, M. 2001 Viscosity of magmas containing highly deformable bubbles. *J. Volcanol. Geotherm. Res.* **105** (1), 19–24.

MINALE, M. 2010 Models for the deformation of a single ellipsoidal drop: a review. *Rheol. Acta* **49** (8), 789–806.

MISBAH, C. 2006 Vacillating breathing and tumbling of vesicles under shear flow. *Phys. Rev. Lett.* **96** (2), 028104.

MWASAME, P., WAGNER, N. & BERIS, A. 2017 On the macroscopic modelling of dilute emulsions under flow. *J. Fluid Mech.* **831**, 433–473.

NOGUCHI, H. & GOMPPER, G. 2007 Swinging and tumbling of fluid vesicles in shear flow. *Phys. Rev. Lett.* **98** (12), 128103.

OLDROYD, J.G. 1953 The elastic and viscous properties of emulsions and suspensions. *Proc. R. Soc. Lond.* A **218** (1132), 122–132.

RIOUAL, F., BIBEN, T. & MISBAH, C. 2004 Analytical analysis of a vesicle tumbling under a shear flow. *Phys. Rev.* E **69** (6), 061914.

ROSCOE, R. 1967 On the rheology of a suspension of viscoelastic spheres in a viscous liquid. *J. Fluid Mech.* **28** (2), 273–293.

SINGH, A. & NOTT, P.R. 2000 Normal stresses and microstructure in bounded sheared suspensions via Stokesian dynamics simulations. *J. Fluid Mech.* **412**, 279–301.

SINGH, A. & NOTT, P.R. 2003 Experimental measurements of the normal stresses in sheared Stokesian suspensions. *J. Fluid Mech.* **490**, 293–320.

SNOOK, B., DAVIDSON, L.M., BUTLER, J.E., POULIQUEN, O. & GUAZZELLI, E. 2014 Normal stress differences in suspensions of rigid fibres. *J. Fluid Mech.* **758**, 486–507.

STONE, H.A. 1994 Dynamics of drop deformation and breakup in viscous fluids. *Annu. Rev. Fluid Mech.* **26** (1), 65–102.

VAN DER WERFF, J.C. & DE KRUIF, C.G. 1989 Hard-sphere colloidal dispersions: the scaling of rheological properties with particle size, volume fraction, and shear rate. *J. Rheol.* **33** (3), 421–454.

VLAHOVSKA, P.M., PODGORSKI, T. & MISBAH, C. 2009 Vesicles and red blood cells in flow: from individual dynamics to rheology. *C. R. Phys.* **10** (8), 775–789.

WALTER, J., SALSAC, A.-V. & BARTHES-BIESEL, D. 2011 Ellipsoidal capsules in simple shear flow: prolate versus oblate initial shapes. *J. Fluid Mech.* **676**, 318–347.

WEI, Q., YOUNG, J., HOLLE, A., LI, J., BIEBACK, K., INMAN, G., SPATZ, J.P. & CAVALCANTI-ADAM, E.A. 2020 Soft hydrogels for balancing cell proliferation and differentiation. *ACS Biomater. Sci. Engng* **6** (8), 4687–4701.

WETZEL, E.D. & TUCKER, C.L. 2001 Droplet deformation in dispersions with unequal viscosities and zero interfacial tension. *J. Fluid Mech.* **426**, 199–228.

ZARRAGA, I.E., HILL, D.A. & LEIGHTON JR., D.T. 2000 The characterization of the total stress of concentrated suspensions of noncolloidal spheres in newtonian fluids. *J. Rheol.* **44** (2), 185–220.

ZHAO, H. & SHAQFEH, E.S.G. 2011 The dynamics of a vesicle in simple shear flow. *J. Fluid Mech.* **674**, 578–604.